Exploring the AGN-merger connection in Arp 245 I: Nuclear star formation and gas outflow in NGC 2992

Muryel Guolo-Pereira,[1][*] Daniel Ruschel-Dutra,[1] Thaisa Storchi-Bergmann,[2] Allan Schnorr-Müller [ORCID],[2] Roberto Cid Fernandes [ORCID],[1] Guilherme Couto [ORCID],[3] Natacha Dametto[3] and Jose A. Hernandez-Jimenez [ORCID][4]

[1]*Departamento de Física – CFM – Universidade Federal de Santa Catarina, 476, 88040-900 Florianópolis, SC, Brazil*
[2]*Departamento de Astronomia, Universidade Federal do Rio Grande do, Sul. Av. Bento Goncalves 9500, 91501-970 Porto Alegre, RS, Brazil*
[3]*Centro de Astronomía (CITEVA), Universidad de Antofagasta, Avenida Angamos 601, 1270-300 Antofagasta, Chile*
[4]*Departamento de Ciencias Físicas, Universidad Andrés Bello, Fernández Concha 700, Las Condes, 7550-196 Santiago, Chile*

ABSTRACT

Galaxy mergers are central to our understanding of galaxy formation, especially within the context of hierarchical models. Besides having a large impact on the star formation history, mergers are also able to influence gas motions at the centre of galaxies and trigger an active galactic nucleus (AGN). In this paper, we present a case study of the Seyfert galaxy NGC 2992, which together with NGC 2993 forms the early-stage merger system Arp 245. Using Gemini Multi-Object Spectrograph integral field unit data from the inner 1.1 kpc of the galaxy, we were able to spatially resolve the stellar populations, the ionization mechanism, and kinematics of ionized gas. From full spectral synthesis, we found that the stellar population is primarily composed by old metal-rich stars ($t \geq 1.4$ Gyr, $Z \geq 2.0\,Z_\odot$), with a contribution of at most 30 per cent of the light from a young and metal-poor population ($t \leq 100$ Myr, $Z \leq 1.0\,Z_\odot$). We detect H α and H β emission from the broad-line region with a full width at half-maximum of $\sim$2000 km s^{-1}. The narrow-line region kinematics presents two main components: one from gas orbiting the galaxy disc and a blueshifted (velocity ≈ -200 km s^{-1}) outflow, possibly correlated with the radio emission, with mass outflow rate of $\sim$2 M$_\odot$ yr^{-1} and a kinematic power of $\sim 2 \times 10^{40}$ erg s^{-1} ($\dot{E}_{out}/L_{bol} \approx 0.2$ per cent). We also show even though the main ionization mechanism is the AGN radiation, ionization by young stars and shocks may also contribute to the emission line ratios presented in the innermost region of the galaxy.

Key words: galaxies: individual: Arp 245, NGC 2992 – galaxies: interactions – galaxies: kinematics and dynamics – galaxies: Seyfert – galaxies: stellar content.

1 INTRODUCTION

The vast majority of galaxies with a spheroid host a supermassive black hole (SMBH) in their centres, with a mass range of $\sim 10^6$–10^{10} M$_\odot$. In some galaxies, these objects are active and emit intense radiation due to the accretion of matter on to the SMBH through an inner region called accretion disc (Begelman, Blandford & Rees 1984; Peterson et al. 1998; Event Horizon Telescope Collaboration 2019). Active galactic nuclei (AGNs) in Seyfert galaxies are classified as types 1 and 2, depending on the presence of broad emission lines of the Balmer series, with intermediate types between these two also possible; these broad lines are produced in a region called broad-line region (BLR).

The importance of AGN in the evolution of the host galaxy is not completely understood, but there is evidence pointing to a co-evolution scenario between the two. The M_{BH}–σ_* relation (Ferrarese & Merritt 2000; Kormendy & Ho 2013) – which relates the mass of the SMBH with the stellar velocity dispersion in the galactic bulge – and the simultaneous peak between star formation rate (SFR) and SMBH accretion rate in cosmological studies at $z \approx$ 2 (Silverman et al. 2008; Madau & Dickinson 2014) are some of the indications towards a causal connection between host galaxy evolution and of its SMBH.

The energy released by the AGN in the form of radiation, winds, or radio plasma jets is known to impact on the interstellar medium of the host galaxy. All these processes are collectively known as feedback. The role of such AGN feedback in the evolution of galaxies, however, is still a subject of ongoing debate. AGN feedback may be a key factor in quenching star formation, mainly in the late stages of the host galaxy's evolution (Di Matteo, Springel & Hernquist 2005; Croton et al. 2006). In fact, large-scale hydrodynamic simulations of galaxy formation are not able to reproduce observed properties of massive galaxies if AGN feedback models are not included (Springel et al. 2005; Bullock & Boylan-Kolchin 2017) in which these processes are responsible for suppressing the growth of the most massive galaxies by heating and expelling the gas that would form more stars. Powerful AGN-driven winds are a possible mechanism for preventing further growth of the host galaxy. These winds can have outflow velocities as high as 1000 km s^{-1} (Rupke & Veilleux 2011; Greene, Zakamska & Smith 2012) and as low as well $\approx$100–200 km s^{-1}, with mass outflow rates in nearby galaxies averaging at a few solar masses per year (e.g. Riffel & Storchi-Bergmann 2011; Crenshaw et al. 2015; Revalski et al. 2018).

[*] E-mail: muryel@astro.ufsc.br

Theoretical studies suggest large-scale events like major mergers are the dominant processes leading to SMBH growth at high masses (Menci et al. 2014). At high redshifts ($z > 2$), major mergers have also been proposed as fuelling mechanisms of the fastest-growing SMBHs (Treister et al. 2012). A major merger can destabilize large quantities of gas, driving massive inflows towards the nuclear region of galaxies and triggering bursts of star formation and nuclear activity (Hopkins & Quataert 2010; Blumenthal & Barnes 2018). Many studies have found that the most luminous AGNs are preferentially hosted by galaxy mergers (Schawinski et al. 2010; Glikman et al. 2015; Fan et al. 2016). At lower luminosities, several studies have found a higher incidence of galaxies with signatures of interactions in AGN hosts as compared to control samples (Koss et al. 2010) and particularly in close galaxy pairs (Ellison et al. 2011; Satyapal et al. 2014) suggesting kinematic pairs are conducive environments for black hole growth.

One possible consequence of gas inflow is the circumnuclear star formation (Hopkins et al. 2008; Hopkins & Quataert 2010). Such merger-driven inflows can both increase the star formation rate (Ellison et al. 2013; Pan et al. 2019) and modify the metallicities gradients of the galaxies (Barrera-Ballesteros et al. 2015). However, classical emission-line SFR probes (e.g. Kennicutt 1998) and metallicity calibrations (e.g. Alloin et al. 1979; Pettini & Pagel 2004) cannot be applied to active galaxies, due to the contamination of the AGN ionization to the emission lines. In this way, the use of stellar populations synthesis, by performing full spectral fitting, can reveal clues on the star formation history (SFH) and chemical evolution of AGN host galaxies and its content.

In this context, we present high spatial and spectral resolution optical IFU observations of the inner 1.1 kpc of NGC 2992. NGC 2992 is a nearby interacting Seyfert galaxy seen almost edge-on ($i \sim 70°$, Marquez et al. 1998) at a distance, as measured using the Tully–Fisher relation, of 38 Mpc (Theureau et al. 2007), which translates into a projected angular scale of $\sim$150 pc arcsec^{-1}. Alongside with the starburst galaxy NGC 2993 and the tidal dwarf galaxy A245N, it forms the system Arp 245. Using hydrodynamic simulations, Duc et al. (2000) reported the system is currently at an early stage of the interaction, about $\approx$100 Myr after pericentre passage. Nevertheless, tidal tails have already developed, which can be seen by optical images (Fig. 1), in CO and H I lines (Duc et al. 2000) and infrared (IR) images (García-Bernete et al. 2015).

The galaxy nuclear activity has been the subject of several studies, partly due to its variability as seen both in X-rays and in the optical (Trippe et al. 2008), even leading to changes in spectral classification. Early spectra published by Shuder (1980), Veron et al. (1980), and Ward et al. (1980) all show the presence of a weak broad Hα component, originated in the BLR, but no detectable corresponding broad Hβ component, leading to its original classification as a Seyfert 1.9. Observations from 1994 (Allen et al. 1999), however, display no broad Hα component, thus having the classification of Seyfert 2. Gilli et al. (2000) reported a broad Hα emission again, just to disappear once again when observed in 2006 by Trippe, Crenshaw & Dietrich (2008). More recently Schnorr-Müller et al. (2016), after subtracting the narrow component, were able to detect the broad Hβ component for the first time, then classifying the galaxy as a Seyfert 1.8.

In the radio, 6 cm observations show a double lobe 8-shaped structure of about 8 arcsec ($\sim$1 kpc) extension to the north-west and south-east of the galaxy, along position angle (PA) of $-26°$ (Ulvestad & Wilson 1984). From IR observations, Chapman et al. (2000) suggest the best interpretation is that this structure is related to expanding plasma bubbles, possibly carried by internal jets from

the AGN. More recently, using radio polarimetry, Irwin et al. (2017) found another double-lobed radio morphology within its spiral disc, which was revealed in linearly polarized emission but not in total intensity emission. This second structure by Irwin et al. (2017) is much more extended than the one found by Ulvestad & Wilson (1984) reaching several kpcs from the nucleus, being interpreted by the authors as a relic of an earlier episode of AGN activity.

NGC 2992 gas kinematics is complex as found by several long slit spectroscopy studies (e.g. Marquez et al. 1998; Veilleux, Shopbell & Miller 2001) as well as by several integral field unit (IFU) observations (García-Lorenzo, Arribas & Mediavilla 2001; Friedrich et al. 2010; Müller-Sánchez et al. 2011). These observations show, at most positions, the presence of a double component line profile. While one component follows the galaxy rotation curve, the other is interpreted as outflowing gas by the authors. Using The Multi Unit Spectroscopic Explorer (MUSE; Bacon et al. 2010) at the Very Large Telescope (VLT), Mingozzi et al. (2019) clearly show the presence of a kpc scale, bipolar outflow with a large opening angle.

This paper is the first in a series that will explore the possible connection between merger and AGN in Arp 245. In this first paper, we analyse both the stellar populations and the properties of the ionized gas of NGC 2992, in order to better understand the physical conditions of the nuclear region and the mutual role of nuclear activity and the interaction may play. In the next papers, we will explore both the effects of the interaction in NGC 2993 using observations and the possible triggering of the AGN during the merger using a modern version of the hydrodynamics simulations by Duc et al. (2000).

This paper is organized as follows: in Section 2, we describe the observations and data reduction; in Section 3, we present the stellar populations synthesis and its spatial distribution; the ionized gas kinematics is described in Section 4; ionization mechanisms are discussed in Section 5; Section 6 presents our discussion of the main results and their significance; and finally Section 7 contains our conclusions.

2 OBSERVATIONS AND DATA REDUCTION

This work is mostly based on data obtained with the IFU of the Gemini Multi Object Spectrograph (GMOS) at the Gemini South telescope on the night of 2018 February 15 (Gemini project GS-2018A-Q-208, P.I. Ruschel-Dutra). The observations consisted of two adjacent IFU fields (covering 5 arcsec × 3.5 arcsec each). The fields are slightly offset, both in right ascension (RA) and declination (Dec.), in order to increase the field of view (FoV) and cover a larger portion of the galaxy plane. For each IFU field, there are six exposures, with an integration time of 560 s each. Each science observation is accompanied by a 5 × 1.75 arcsec sky observation for atmospheric lines removal.

The spatial resolution is limited by seeing, which was at 0.8 arcsec during the observations, corresponding to 120 pc at the galaxy. The observed spectra covered a range from 4075 to 7285 Å; with an instrumental dispersion $\sigma_{instr} \approx 40$ km s^{-1}, obtained from the copper–argon arc lamp lines.

The reduction procedures were performed using the Gmos Ifu REDuction Suite (GIREDS).[1] The process comprised the usual steps: bias subtraction, flat-fielding, trimming, wavelength calibration, telluric emission subtraction, relative flux calibration, the building of the data cubes, and finally the registering and combination of the 12 individual exposures. The final cube was built with a spatial

---

[1]GIREDS is a set of python scripts to automate the reduction of GMOS IFU data, available at GitHub.
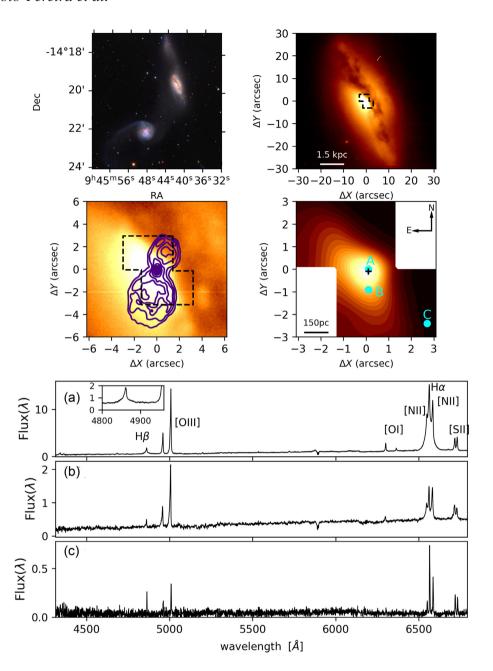
Figure 1. Top left: LRGB image composition of Arp 245 from Block (2011). Top right: GMOS *r*'-band acquisition image of NGC 2992. Middle left: Zoomed acquisition image, and the Ulvestad & Wilson (1984) radio emission in purple (contours: 3, 6, 9, 15, 30, 50, 70, 90 per cent of the peak of 7.2 mJy). The dashed rectangles show the two IFU FoV's. Middle right: IFU continuum mean flux in the FoV. The black cross represents the continuum nuclear position in all figures of the paper. All maps of the paper were smoothed using a Gaussian kernel with FHWM with half of the spatial resolution, see Section 2. Bottom, from top to bottom: Spectra corresponding to the regions marked as A, B, and C, with spectral flux density in units of 10^{-15} erg s^{-1} cm^{-2} Å^{-1}. North is up and East to the left in this and all figures of the paper.

sampling of 0.1 arcsec × 0.1 arcsec, resulting in an FoV with ≈2800 spaxels. After cropping the borders and superimposing the FoVs, it results in a total useful combined FoV, with total angular coverage of 29 arcsec² around the nucleus. The combined FoV is centred at RA = 9^{h}45^{m}42^s and Dec. = −14°9'3", while the continuum peak is shifted at ΔRA = 0.1 arcsec and ΔDec. = −0.1 arcsec.

Many Gemini data cubes show certain 'instrumental fingerprints', in the form of vertical stripes in the reconstructed data cube. Such features also have specific spectral signatures. In order to identify and remove these instrumental features, we use a technique based on principal component analysis (PCA; Menezes, Steiner & Ricci 2014).

The fingerprint removal is fundamental for the stellar population synthesis because its effect is more apparent for lower instrumental counts. The data cube spectra were corrected for Galactic extinction using the Cardelli, Clayton & Mathis (1989) extinction curve (CCM) for an $A_V = 0.166$ (Schlafly & Finkbeiner 2011) and by Doppler effect using the radial velocity of 2345 km s^{-1} (see Section 4).

We show in the upper panel of Fig. 1 an LRGB image of the Arp 245 system (left) and the acquisition image taken with a *r*' filter (right). In the middle panel, we show a zoomed version of the acquisition image superimposed with the Ulvestad & Wilson (1984) figure of 8-shaped radio emission of the galaxy (left) and the mean

continuum flux in the IFU's FoV (right), while in the bottom panels we show three sample spectra from representative regions marked, respectively from top to bottom, A, B, and C. The prominent dust lane seen in the acquisition image, and in the stellar continuum image from the IFU, has a reported A_V greater than 3 (Colina et al. 1987; Schnorr-Müller et al. 2016). Spectra from this region of high extinction have no measurable stellar component above the noise level, as exemplified by the spectrum extracted from C. The nuclear spectrum shows a broad Hα component, and a faint broad Hβ is also present, in contrast with its original Seyfert 1.9 classification but in agreement with its the current state, Seyfert 1.8, proposed by Schnorr-Müller et al. (2016).

3 STELLAR POPULATIONS

In order to obtain the spatially resolved SFH, and to fit the gas emission features, free from the stellar population contamination, we performed stellar population synthesis on the data cube by employing the STARLIGHT full spectra fitting code (Cid Fernandes et al. 2005).

Briefly, STARLIGHT fits an observed stellar spectrum O_λ with a model M_λ built from a linear combination of N spectral components. Dust attenuation is treated as if due to a foreground screen and parametrized by the V-band extinction A_V. Stellar kinematics is modelled with a Gaussian line-of-sight velocity distribution centred at velocity v_*, and with a dispersion σ_*. Besides the model spectrum M_λ, the code outputs the corresponding values of A_V, $v_\star$, $\sigma_\star$, and a population vector $\vec{x}$ containing the percentage contribution of each base population to the flux at a chosen normalization wavelength λ_0, which in our fits was chosen as $\lambda_0 = 5500$ Å. The code minimizes the χ^2 of the fit, though a more convenient and intuitive figure of merit to assess the quality of the fit is through *adev* parameter, defined as the mean value of $|O_\lambda - M_\lambda|/O_\lambda$ over the fitted wavelengths.

We note that, while there are many different spectral fitting codes and techniques available, cross-comparison of these various techniques have shown to yield rather consistent results (e.g. Koleva et al. 2008; Ferré-Mateu et al. 2012; Maksym et al. 2014; Mentz et al. 2016; Cid Fernandes 2018). Therefore, rather than trying different fitting codes, we chose to maintain STARLIGHT and investigate the differences introduced by the choice of models and stellar libraries, which are known to produce variations in the recovered properties (e.g. Chen et al. 2010; Maraston & Strömbäck 2011; Wilkinson et al. 2017; Baldwin et al. 2018; Dametto et al. 2019).

3.1 Evolutionary models, stellar libraries, and featureless continuum

This section discusses the stellar population models and stellar libraries used in this work, and how we can account for the contribution of a featureless continuum due to the AGN in NGC 2992.

The key ingredients in the stellar population synthesis method are the spectral base elements, i.e. those spectra available to the fitting code to combine in order to recover the galaxy properties. The base elements are, usually, simple stellar population (SSP), i.e. a collection of stars with same age and metallicity, taken from an evolutionary model that are constructed using a stellar spectra library and an initial mass function (IMF).

In this work, we have used SSPs from two models: Bruzual & Charlot (2003, BC03), which uses the STELIB (Le Borgne et al. 2003) spectral library, and Maraston & Strömbäck (2011, M11), which employs the MILES (Sánchez-Blázquez et al. 2006) spectral library. For both models/libraries, we use the same Chabrier (2003) IMF and instantaneous star formation bursts. We found varying the

IMF produces only minor variations in the recovered SFH when compared to the changes introduced by using distinct models. The former is outside the scope of this work, and we refer the reader interested in this particular effect to Chen et al. (2010), Ge et al. (2019), and references therein. From the SSPs provided by BC03, we choose a set of 45 representative elements divided into three metallicities (0.2, 1.0, 2.5 Z$_\odot$) and an age range covering from t(Gyr) = 0.001 to t(Gyr) = 13. From those available by M11 with the MILES library, we chose a set of 40 SSPs with age and metallicity coverage as similar as possible to the BC03 ones: three metallicities (0.5, 1.0, 2.0 Z$_\odot$) and ages ranging from t(Gyr) = 0.007 to t(Gyr) = 13. The complete list of SSPs used from each model is shown in Table 1. It is important to mention that the MILES Library does not provide metal-poor stars ($Z = 0.5$ Z$_\odot$) younger than 55 Myr (0.055 Gyr), and neither metal-rich stars ($Z = 2.0$ Z$_\odot$) younger than 100 Myr (0.1 Gyr), while BC03/STELIB provide the same age range for the three metallicities (see Table 1).

We define a reduced population vector with three age ranges: $t < 100$ Myr; 100 Myr $\leq t \leq 1.4$ Gyr; and $t > 1.4$ Gyr, to obtain a more robust description of the SFH than that obtained with the full population vector (see e.g. Cid Fernandes et al. 2005), as well as to facilitate the visualization of the spatially resolved fit results. The population vector components are denoted by x_Y, x_I, and x_O, where `Y', `I', and `O' stands for young, intermediate, and old, respectively. The division in a reduced population vector has been used in several works in stellar population synthesis (e.g. Cid Fernandes et al. 2005; Riffel et al. 2010a; Cid Fernandes et al. 2013; González Delgado et al. 2015; Mallmann et al. 2018), while the range values may be slightly distinct from one another, the ones adopted here are the most common. Also, for the young population the cutting value of 100 Myr is the estimated age of the pericentre passage between NGC 2992 and its companion (Duc et al. 2000).

When dealing with stellar populations in Seyfert galaxies, a power-law ($F_\lambda \propto \lambda^{-\alpha}$) featureless continuum (FC) should be added to the spectral base (Koski 1978) to account for the AGN emission. Values for α are between 0.5 and 2.0 (Osterbrock & Ferland 2006), with many authors working with large samples of galaxies assuming a general value of $\alpha = 1.5$ (Raimann et al. 2003; Storchi-Bergmann et al. 2003; Cid Fernandes et al. 2004; Mallmann et al. 2018). Since this work is focused on a single object, we propose a method to specifically fit the α index for the optical spectrum of NGC 2992. We extracted two integrated spectra: an inner one, hereafter $S(\lambda)$, defined as the sum of spectra within a circular region with radius of 0.4 arcsec, and an external one, $E(\lambda)$, in an annulus with inner radius of 1 arcsec and outer radius of 1.4 arcsec, both centred at the peak of continuum emission. We model the $S(\lambda)$ spectrum as a combination of $E(\lambda)$ and a power-law FC ($F_\lambda \propto \lambda^{-\alpha}$), both reddened by the same factor and normalized in the same wavelength, $\lambda_0 = 5500$ Å, as follows:

$$\left(\frac{S_m(\lambda)}{S_m(\lambda_0)}\right) = \left[(1 - p)\left(\frac{E(\lambda)}{E(\lambda_0)}\right) + p\left(\frac{\lambda}{\lambda_0}\right)^{-\alpha}\right]$$
$$\times 10^{-0.4\delta A_V q_\lambda}, \tag{1}$$

where $S_m(\lambda)$ is the model spectrum, p is the fraction contribution of the FC, and δA_V is the difference in extinction between the $S(\lambda)$ and $E(\lambda)$ regions. The values that minimize the residuals between $S(\lambda)$ and $S_m(\lambda)$ are $p = 0.23$, $\delta A_V = 2.2$, and $\alpha = 1.7$.

It should be noted we are oversimplifying by assuming that $S(\lambda)$ is the combination of $E(\lambda)$ and an FC, i.e. the stellar spectrum of both are the same. However, we argue this is just a method to get a data-based value for α, instead of just assuming a fixed value which

Table 1. SSPs used in the stellar population synthesis.

Model	BC03			M11		
Spectral library	STELIB			MILES		
Metallicity ($Z_\odot$)	0.2	1.0	2.5	0.5	1.0	2.0
Ages (Gyr)	0.001, 0.003, 0.005, 0.01, 0.025, 0.04, 0.1, 0.3, 0.6, 0.9, 1.5, 3.0, 5.0, 11.0, 13.0			0.055, 0.065, 0.075, 0.085, 0.1, 0.15, 0.3, 0.6, 0.9	0.007, 00008, 0.009, 0.01, 0.015, 0.025, 0.04, 0.055, 0.065, 0.075, 0.085, 0.1, 0.15, 0.3, 0.9, 1.5, 3.0, 5.0, 11.0, 13.0	0.1, 0.15, 0.3, 0.6, 0.9, 1.5, 3.0, 5.0, 11.0, 13.0

is even less physically justified. Also, no further interpretation will be given in this regard besides the adoption of this α value to produce the FC base element.[2]

3.2 Spatially resolved stellar populations synthesis

In order to perform the spatially resolved stellar synthesis with enough signal-to-noise ratio (S/N) we employed the Voronoi tessellation technique (Cappellari & Copin 2003) in our data cube, with an S/N target set to 20. Results from Cid Fernandes et al. (2005) show at this level STARLIGHT is able to reliably recover input parameters. Some spectra, however, failed to reach the desired S/N, even when combining several tens of spaxels, specifically those obscured by the galaxy's dust lane. Henceforward, we will just analyse and show the results for those voronoi zones that the combined-spectra has S/N $\geq$ 10, relying again on Cid Fernandes et al. (2005) tests that show it to be the minimum value to the reliability of the code. STARLIGHT measures the S/N as the ratio between the mean and the root-mean-squared (RMS) flux in a user-selected region of the spectrum (which should be as featureless as possible), the range adopted here is a $\Delta\lambda = 20$ Å wide window around the normalization wavelength as measured from the combined-spectra of the Voronoi zone.

In order to be able to explore both the effects of the FC component and the change of model/library, we run the STARLIGHT code in the spaxels of the binned cube using three distinct spectral bases:

(i) *BC03*: Only stellar SSP components from the BC03/STELIB models, see Table 1 for ages and metallicities.

(ii) *BC03 + FC*: Same as BC03 stellar SSPs, with the addition of an FC component ($F_\lambda \propto \lambda^{-1.7}$) to the spectral base.

(iii) *M11 + FC*: Stellar SSP components from M11/MILES, see Table 1 for ages and metallicities, in addition to the FC component.

Since the effects of the presence/absence of FC component can be tested comparing *BC03* with *BC03 + FC*, and the change of model/library is explored comparing *BC03 + FC* with *M11 + FC*, we did not find necessary to test the synthesis using *M11* without FC, therefore we kept our analyse within these three configurations.

The FC component is available for STARLIGHT only in the spaxels of the inner 1.1 arcsec,[3] which equals 3σ of the Gaussian point spread function. The reason for not allowing the FC to be used throughout the field is that there is a high level of degeneracy between the FC and a young reddened population [further discussion in Cid Fernandes & González Delgado (2010) and the next section], and also because there is no physical reason to have an FC emission outside the nucleus since it is emitted by the spatially unresolved accretion disc. We will call the percentage contribution of the FC to total light of a spaxel as x_{agn}. During the synthesis all the emission lines were masked (see Fig. 2), the mask is the same in all spaxels with exception to the central ones ($r < 1.1$ arcsec) where Hβ and [N II] $+$ Hα masks are broader. The sum of x_Y, x_I, x_O, x_{agn} values is always 100 per cent for all spaxels.

The maps of the recovered properties from the three distinct bases are shown in Figs A1, A2, and A3 in Appendix A. These figures show the maps for x_Y, x_I, x_O, x_{agn}, A_V, the light-weighted stellar mean age $\langle \log t_* \rangle$ defined as

$$\langle \log t_* \rangle = \frac{\sum_{j=1}^{N_*} x_j \log(t_j)}{\sum_{j=1}^{N_*} x_j}, \qquad (2)$$

where x_j are the elements of the population vector $\vec{x}$, i.e. the fraction contribution of each component to the total light, t_j is the ages of j-th component, and N_* is the number of stellar spectra in the base (SSPs). The figures in Appendix A also show the light-weighted stellar mean metallicity $\langle Z \rangle$ for each reduced population vector component x_Y, x_I, and x_O, respectively $\langle Z \rangle_Y$, $\langle Z \rangle_I$, and $\langle Z \rangle_O$, defined as

$$\langle Z \rangle = \frac{\sum_{j=t_0}^{t_f} x_j z_j}{\sum_{j=t_0}^{t_f} x_j} \qquad (3)$$
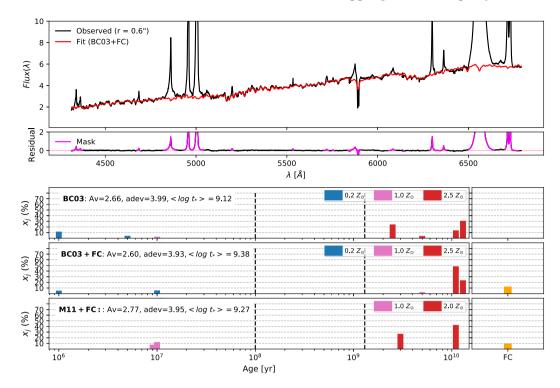
where t_0 and t_f are respectively the lower and upper age limit of the reduced population vector components as defined in the previous section.

The upper panel of Fig. 2 shows an example fit for a spaxel at $r = 0.6$ arcsec, the residuals between the observed and the fitted spectra and the emission line mask. At the bottom panels, the age/metallicity/FC decomposition for the three syntheses are shown as an example of the small differences resulting from the change of spectral base (see Sections 3.3 and 3.4).

In Fig. 3, we show the radial profiles of x_Y, x_I, x_O, x_{agn}, and $\langle \log t_* \rangle$, in bins of 0.45 arcsec ($\approx$70 pc), with points representing the median, and the coloured region represents the 25 and 75 percentiles of the azimuthal distribution for the given radial bin. In Fig. 4, we show the

---

[2]Further validation of this approximation will be presented throughout the paper, once the almost constant radial profiles shown in Fig. 3 is taken into account, and the inferred stellar A_V estimates, roughly consistent with those derived from the Balmer decrement [see also e.g. fig. A.1 in Mingozzi et al. (2019) for consistent results] will be presented in Appendices A and B.

[3]The radius (r) $= 0.0$ is set as the peak of the continuum emission.

Figure 2. Example of stellar population synthesis fit. Top: Observed (black) and synthetic (red) spectra both in units of 10^{-15} erg s^{-1} cm^{-2} Å^{-1} in a spaxel at radius equal to 0.6 arcsec. Middle: Residual between the observed and synthetic spectra, masked emission lines are shown in purple. Bottom: Age/metallicity and FC decomposition for the three synthesis, *BC03*, *BC03 + FC*, and *M11 + FC*. The dashed lines show the division between x_Y, x_I, and x_O SSPs.

values of $\langle Z \rangle$ for each one of the bases integrated over the entire FoV.

In general terms, the presence of a large contribution of old metal-rich SSPs and a smaller, but significant, contribution of young metal-poor stars seems to be independent of the presence of an FC component, or the change of model/library. The detailed analyses of the differences caused by the distinct spectral bases available to the code will be better explored in the sections below.

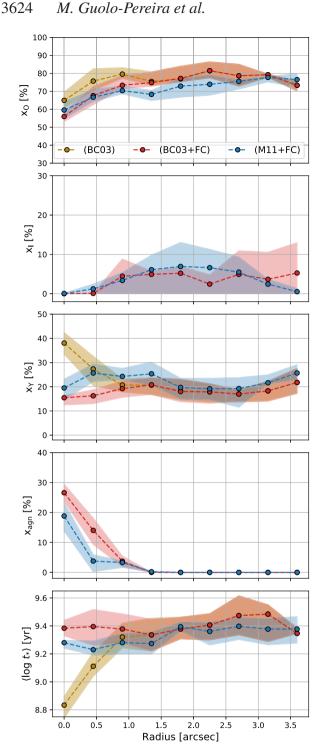### 3.3 The FC component usage: comparing BC03 and BC03 + FC

As shown by Fig. 3, the differences in the *BC03* and *BC03 + FC* synthesis are seen only at the inner spaxels and are linked to the presence of the FC component in the spectral base. For the external spaxels ($r > 1.1$ arcsec), where only BC03 stellar components are used in both synthesis, the recovered properties are identical, as one would expect. In the external spaxels, the x_O values range between 75 per cent and 85 per cent, with all spaxels having supersolar mean metallicity, $\langle Z \rangle_O > 1.5 \, Z_\odot$, and the majority of them being close to the upper limit of the models, $\langle Z \rangle_O \approx 2.5 \, Z_\odot$. The x_Y values are between 15 per cent and 25 per cent, with most spaxels having a sub-solar mean metallicity, $\langle Z \rangle_Y \leq 1.0 \, Z_\odot$, with a considerable portion of them at the lower limit of the model, i.e. $\langle Z \rangle_Y = 0.2 \, Z_\odot$. Some properties are identical in all runs even at the inner spaxels, A_V is very high in the innermost spaxels ($A_V > 3$ mag) declining rapidly to $A_V \approx 2.5$ mag and reaching 1.5 mag at the border spaxels (A_V map shown at Appendix A). Similarly, the contribution from intermediate SSPs, x_I, is null at most spaxels and reaches a maximum value between 10 and 20 per cent in very few regions.

Comparing the inner spaxels of *BC03* and *BC03 + FC*, we see that the presence of an FC component in the base causes a decrease in x_O by just a few per cent. Larger differences, however, are seen in the

contribution from young stars, especially where an FC component is not available (*BC03*). In this case, there is a sharp increase in x_Y from a steady 20 per cent at $r > 1$ arcsec to more than 40 per cent at the centre. On the other hand, the (*BC03 + FC*) base produces a roughly constant x_Y at $r < 1.0$ arcsec, while x_{agn} increases from ~0 per cent at 1.0 arcsec to ~20 per cent in the innermost spaxels. This effect is caused by the above-mentioned degeneracy between an FC spectrum and a young-reddened SSP (Cid Fernandes et al. 2004; Cid Fernandes & González Delgado 2010). As shown by Cardoso, Gomes & Papaderos (2017), fitting a spectrum that contains an AGN power law-like continuum with only stellar components causes the solution to have an excess of young populations, which leads to a drop in the $\langle \log t_* \rangle$ (see the bottom panel of Fig. 3). Although such degeneracy can cast some doubts in the exact values of the x_Y and x_{agn} decomposition in *BC03 + FC*, the fact that the solution at the centre has x_Y values compatible with the ones of the external regions of the FoV, and that the FC component contribution follows a radial profile compatible with an unresolved source (i.e. increasing from $x_{agn} \approx 0$ per cent to $x_{agn} \approx 20$ per cent at the continuum peak) is strong evidence in favour of the existence of an FC emission in NGC 2992.
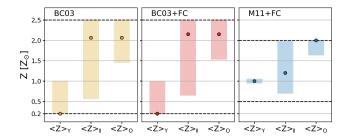
3.4 Decomposition stability: comparing BC03/STELIB and M11/MILES

In this section, we discuss differences in the recovered properties between *BC03 + FC* and *M11 + FC* bases and their derivations. We do not intend to make a detailed analysis of the models and its derivations, nor to suggest one is a better choice than the other for use with this type of data. Such discussions can be found in other studies (e.g. Baldwin et al. 2018; Ge et al. 2019). Instead, we merely want to test the stability of the inferred stellar properties with changes in models.

Figure 3. Radial profiles of the recovered properties for *BC03* (gold), *BC03 + FC* (red), and *M11 + FC* (blue) in bins of 0.45 arcsec (∼70 pc). From top to bottom: Per cent contribution to the total light from young (x_Y), intermediate (x_I), and old (x_O) SSPs, from the FC (x_{agn}) and the light-weighed mean stellar age ($\langle \log t_* \rangle$). x_{agn} is null for *BC03* by definition. The x_I values for *BC03* are not shown, however they are exactly the same as *BC03 + FC*.

Besides the distinct stellar libraries used in these model libraries, they also employ different evolutionary prescriptions (see Conroy 2013, for a review on stellar evolutionary models). BC03 is constructed using the isochrone synthesis approach, while M11 uses the fuel consumption theory. The treatment of the thermally pulsing asymptotic giant branch (TP-AGB) phase is also a major topic of disagreement between different models. For example, Dametto

Figure 4. Values of $\langle Z \rangle_Y$, $\langle Z \rangle_I$, and $\langle Z \rangle_O$ integrated over the entire FoV for each base, from left to right, respectively, *BC03*, *BC03 + FC*, and *M11 + FC*. Points are the median values, and the coloured bars are the 25th and 75th percentiles. The dashed black lines show the metallicity limit for each of the models.

et al. (2019) found a relative excess of young populations and lack of intermediate-age components when near-infrared (NIR) stellar populations synthesis are performed with BC03 SSPs, favouring results achieved with the M11 models. Nevertheless, these effects are much more important when modelling stellar populations in the NIR, being significantly less relevant in the optical.

Both x_{agn} and A_V are very similar to those obtained with *BC03 + FC*, but the population vectors have notable differences. For instance, x_O values for *M11 + FC* are systematically lower by ∼5–10 per cent than those recovered with *BC03 + FC*, while at the same time both x_Y and x_I are conversely higher for *M11 + FC*. Given the increase of both x_Y and x_I and the decrease in x_O, the light-weighted mean stellar age $\langle \log t_* \rangle$ for *M11 + FC* is systematically lower than for *BC03 + FC* by ∼0.5–0.1 dex, as show in the bottom panel of Fig. 3.

Although there are small differences in age decomposition, the metallicity general pattern seems to be maintained. As can be seen in Fig. 4, the old populations have a supersolar mean metallicity, close to the upper limit of the model ($1.5\,Z_\odot < \langle Z \rangle_O \leq 2.0\,Z_\odot$) and the young populations have a solar to sub-solar mean metallicity ($\langle Z \rangle_Y \leq 1.0\,Z_\odot$), as shown in the middle panels of Fig. 4. However, while the values of $\langle Z \rangle_Y$ in *BC03 + FC* are mostly sub-solar ($\langle Z \rangle_Y < 1.0\,Z_\odot$) the values in *M11 + FC* are all solar ($\langle Z \rangle_Y = 1.0\,Z_\odot$). This discrepancy is probably caused by the fact that the MILES library does not contain SSPs with a sub-solar metallicity younger than 55 Myr (see Table 1). For instance, in the example of Fig. 2, while *BC03* and *BC03 + FC* recover its young populations as a combination of three SSPs with ages of 1, 5, and 10 Myr, the two first with sub-solar metallicity ($Z = 0.2\,Z_\odot$) and the later with solar metallicity ($Z = 1.0\,Z_\odot$), the *M11 + FC* recovers it as both 9 and 10 yr solar metallicity SSPs, and the fitting code would not be able to fit such a young component with lower metallicity precisely because MILES library does not provide an SSPs with $Z = 0.5\,Z_\odot$ younger than 55 Myr. Therefore, we can see these $\langle Z \rangle_Y = 1.0\,Z_\odot$ values in the synthesis using *M11 + FC* base as an upper limit for the young population metallicity.

As mentioned, above, we do not claim any of the three syntheses to be the one that better describes the data. In fact, there are no significant differences in the *adev* parameters among the bases: *adev* values range from 3 per cent at the inner spaxels up to 8 per cent at larger radius. Recovered properties produced with the distinct models present the same general trend (see Section 3.2). However, we argue the bases which include an FC component are more physically justified. Both the large decrease in $\langle \log t_* \rangle$ in the inner spaxels, when this component is ignored, and the fact that the FC components fluxes have a spatial profile characteristic of a point-like source (FWHM ≈ 0.8 arcsec, see Fig. 7) are strong evidence of the existence of an FC like emission in NGC 2992. It is worth mentioning even though we

are not discussing results for the stellar kinematics, we have made sure all the three decompositions were kinematically consistent with each other, and no non-physical value was fitted to v_*, σ_* parameters, which would cause an incorrect subtraction of the continuum used in emission line fitting procedures of the next sections.

4 GAS KINEMATICS

Emission line structure of the central regions of AGN is very complex, often possessing multiple velocity components along the line of sight (e.g. Villar-Martín et al. 2011; Veilleux et al. 2013; McElroy et al. 2015). For the type 1 and intermediate-type AGNs, the presence of both narrow and broad emission lines are seen; these emission lines are believed to come from two distinct parts of the AGN. The first is named the BLR. Its typical size, as deduced from the broad line variability, is 10–100 light-days, therefore it is spatially unresolved by current observations, meaning that its spatial profile is the same as the point spread function (PSF) of the observation. BLR emission is characterized by very broad (1000 km s^{-1} < FWHM < $10\,000$ km s^{-1}) Balmer lines and the absence of forbidden lines (Peterson 1997). In most cases, the line profiles strongly deviate from a Gaussian profile, e.g. NGC 1097 (Schimoia et al. 2015). The second region is the 'narrow-line region' (NLR) which is much larger than the BLR since no clear variation of the narrow emission lines is observed in objects undergoing large variations of the AGN's featureless continuum on time-scales shorter than several years. The NLR is resolved by ground-based observations showing dimensions of 100–1000 pc in most nearby AGNs and up to several kpc's in higher redshift quasars (Bennert et al. 2006; Sun, Greene & Zakamska 2017; Storchi-Bergmann et al. 2018). The NLR emission is characterized by both permitted and forbidden lines with lower velocity dispersion (FWHM < 1000 km s^{-1}), but still broader than emission lines of normal star-forming galaxies. Even the NLR emission lines are sometimes not well fitted by a simple Gaussian profile, given the presence of multiple kinematical components in the line of sight, e.g. gaseous disc rotation, gas outflows and inflows (e.g. Zakamska et al. 2016; Schnorr-Müller et al. 2017).

4.1 Emission line fitting

In order to fit the emission lines in NGC 2992, we use the IFSCUBE package[4] (Ruschel-Dutra 2020). IFSCUBE is a python based software package designed to perform analysis tasks in data cubes of integral field spectroscopy, mainly focused on the fitting of spectral features, such as atomic lines. It allows for multiple combinations of Gaussian and Gauss-Hermite functions, with or without constraints to its parameters. Stellar continuum subtraction, as well as pseudo continuum fitting if necessary, are performed internally, and in this case, we used the residual spectra from the stellar population synthesis performed with STARLIGHT. Initial guesses for the parameters are set for the first spaxel, usually, the one with the highest S/N, and all subsequent spectra use the output of neighbouring successful fits as the initial guess.

When dealing with complex emission, the standard approach is to model the line profile with a combination of Gaussian functions. Visual inspection of our IFU shows distinct velocity components, evidenced by large asymmetries in the line profiles, are present in over one-third of the spectra in the FoV. As a result, we decided to model these components separately and to investigate whether they possessed any meaningful physical information, following previous

works (e.g. Villar-Martín et al. 2011; McElroy et al. 2015; Fischer et al. 2018).

For every fitted emission line, we determined if the multicomponent model was statistically justified, and not a better fit purely by virtue of the extra model parameters, by performing a series of *f*-tests. The *f*-test is a standard statistical test to gauge whether a higher order model is preferable to a simpler model when fitting a particular data set. We set the false rejection probability for the lower order model to 10^{-5}. The higher this threshold is set, the harder it is to justify a more complex model and the more likely it is to be overfitting noise. The reader interested in more detailed analyses and a step-by-step deduction of the application of *f*-test in astrophysics emission line fitting is referred to Freund (1992) and statistical references therein.

As an Intermediate-type Seyfert nucleus, NGC 2992 presents both BLR and NLR emission. The BLR emission lines (Hα and Hβ) are blended with some NLR emission lines (Hα, [N II]λ6548, [N II]λ6583, and Hβ), leading to degeneracies if both NLR and BLR emission lines are fitted, spaxel by spaxel, at the same time with all parameters free. Fortunately, the fact that the BLR is not resolved, i.e. its kinematics and its Balmer decrement (Hα/Hβ) cannot vary spatially, can be used to decrease this degeneracy. Our chosen methodology consists on first fitting an integrated spectrum to fix the BLR emission line profile (kinematics and Balmer decrement), and later using this BLR spectrum as a fixed component, except for the flux, on the spatially resolved NLR fits.

We extracted a spectrum centred at the continuum peak, using a virtual aperture of $3\sigma = 1.1$ arcsec (σ refers to the Gaussian point spread function). In this spectrum we fitted [N II]λ6548, [N II]λ6583, Hα (both BLR and NLR), and Hβ (both BLR and NLR), adding Gaussian components to the emission lines until the addition of a new component does not increase the fitting quality, as measured by the *f*-test described above. The final fit has shown that two Gaussians are necessary to fit each one of the BLR Balmer emission lines. This resulting profile, meaning the superposition of two Gaussian functions, hereafter called as BLR Component, can be seen in panel (1) of Fig. 5, and is characterized by a FWHM$_{BLR} = 2010$ km s^{-1} and a Balmer decrement of (Hα/Hβ)$_{BLR} = 24.2$. These values are in considerable agreement with the ones fitted by Schnorr-Müller et al. (2016), FWHM$_{BLR} = 2192$ km s^{-1} and (Hα/Hβ)$_{BLR} = 19.2$, considering these authors used three Gaussian functions to model the profile and the BLR of NGC 2992 has been shown to vary in a few years period (Trippe et al. 2008).

In order to resolve the kinematics of the NLR and obtain maps of emission line ratios, we fitted the following eight strongest emission lines present in the data cube: Hβ, [O III]λ4959, λ5007, Hα, [N II]λ6548, λ6583, and [S II]λ6716, λ6731. Each emission line was modelled with a set of Gaussian functions. The central wavelength of the Gaussian functions was allowed to vary by up to ± 400 km s^{-1} and the velocity dispersion up to 400 km s^{-1} (FWHM ≈ 1000 km s^{-1}). We added one more set of Gaussians to the fit, meaning that each emission line is modelled by up to two Gaussian components. To reduce the number of free parameters, each set of Gaussians was required to have the same velocity and velocity dispersion (meaning their relative wavelengths were fixed), while their fluxes were allowed to vary. The reason for this is each component represents a kinematically distinct part of the gas, meaning that they may have different ionization states determined by their relative fluxes. This means that, for example, the single-component set of Gaussians fit to the eight emission lines instead of having twenty four (eight lines × three parameters) free parameters, only had nine (a single velocity, v, and velocity dispersion, σ, amplitudes of Hα, Hβ, the two [S II] and the stronger
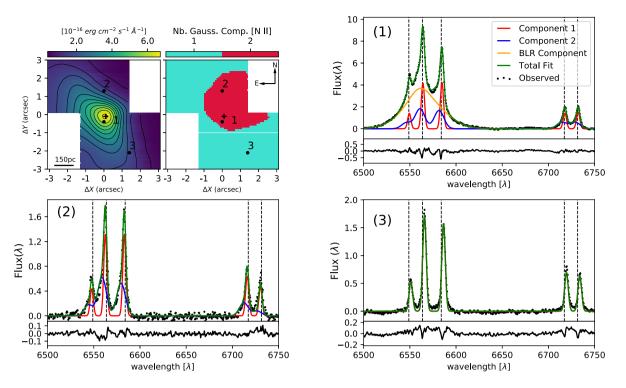
Figure 5. Top left: Map of the continuum emission at $\lambda = 5500$ Å; and map of the preferred number of Gaussian components to the [N II] emission-lines. Top right and bottom: Examples of the Hα, [N II]λ6548, λ6583, and [S II]λ6716, λ6930 emission lines fitting and their residual in distinctly regions of the FoV marked in the maps. The vertical axis units in the panels showing the emission-line profiles are 10^{-15} erg s^{-1} cm^{-2} Å^{-1} and the dashed vertical lines show rest-frame wavelength of the lines.

[N II] and [O III], while the amplitudes of the weaker [N II] and [O III] were set fixed as 1/3 of the stronger ones, as given by their Quantum Mechanics' probabilities (hereafter we call [O III]λ5007 as [O III], [N II]λ6583 as [N II], and the [S II]λ6716, λ6731 as [S II]). As described in the previous paragraph, the BLR component was also included in the fit with only the amplitude as free parameter.

To estimate the uncertainties in the parameters, we performed Monte Carlo simulations, in which Gaussian noise was added to the observed spectrum. One hundred iterations were performed and the estimated uncertainty in each parameter was derived from the standard deviation in all the iterations. The uncertainty maps are presented in Appendix B.

We then applied the *f*-test to each one of the NLR emission lines, spaxel by spaxel, in order to assess if the simple model (single-Gaussian) is enough to fit the data or the more complex model (two Gaussians) is required. The *f*-test results in spatially contiguous regions of the required number of components for each emission line. The maps for [N II] and [O III] emission lines are shown in Figs 5 and 6. The figures also show spectral and emission line fits in selected regions of the FoV.

The maps are not exactly equal for all emission lines, the size of the region in which two components are needed depends on the line S/N,[5] therefore the size is maximum for [O III] (Fig. 6) and Hα (Fig. 11), a little bit smaller for [N II] (Fig. 5) and the [S II] doublets (not shown) and much smaller for the low S/N line, Hβ (not shown). However, the general pattern is the same for all emission lines: the

data are well fitted by a single-Gaussian in most of the FoV, but in a region, from the nucleus to the end of the FoV in the north-west (NW) direction two Gaussians are needed.

As can be seen in both figures, for those spaxels in which the emission lines are well behaved and symmetric, a single-Gaussian function, which we will call Component 1, is enough to fit the data. However, in the spaxels where two components were statistically significant, the profiles show an asymmetry in the form of a blueshifted wing [see panels (1) and (2) in Figs 5 and 6] requiring the addition of a second Gaussian, which we will call Component 2.

In Fig. 7, we show the spatial and radial profile of the BLR component. As expected for an unresolved structure, this component is detected just in the innermost spaxels, with a spatial distribution of a point-like source, equal to that of the stars in the acquisition image (FWHM ≈ 0.8 arcsec, see Section 2); at radii larger than 3σ (1.1 arcsec) it is almost undetectable.

4.2 Rotational and non-rotational components in the NLR

Let us now discuss the spatially resolved properties of the NLR components 1 and 2 and their possible physical interpretation. Component 1 is present in the entire FoV. In the top panels of Fig. 8 we show, from left to right, [O III] flux, velocity dispersion (σ), already corrected by instrumental dispersion. In the middle left panel, we present the radial velocity (v). We show the [O III] flux as an example of the morphology of this component, which is similar to the continuum morphology, with the peak of the emission shifted by only $\sim$0.2 to southwest (SW), with a steep decrease (up to 2 dex) towards the dust lane region. The σ values range from 50 to 100 km s^{-1} and show a very disturbed pattern. The v map shows values from -130 to 120 km s^{-1} and although it presents some disturbance, a rotation

---

[5]Because the *f*-test detection is sensible to how much the second component, the more complex model, stands out from the noise. Therefore in low S/N lines, it is less likely the *f*-test will require a complex model.
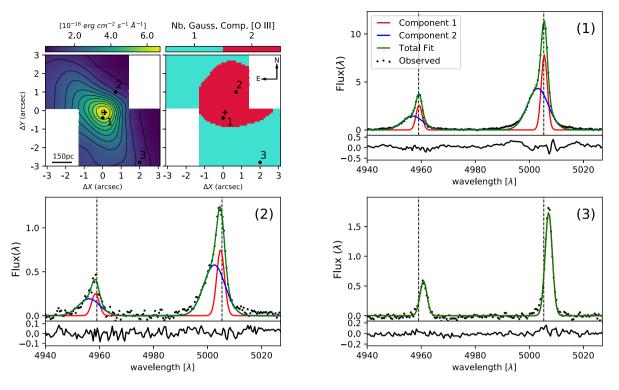
Figure 6. Same as Fig. 5 but for [O III] emission lines.

pattern is clearly discernible, with the SW portion receding and the northeastern (NE) approaching. We have considered the west side of the galaxy is the near one, following the literature (e.g. Marquez et al. 1998; Veilleux et al. 2001); this explains why the emission is seen mainly to the east and less to the west where it is attenuated by the dust lane in the line of sight.

In order to quantify how much the velocity field deviates from a pure rotation and to derive both the major axis PA and the inclination of disc, we fit the Bertola et al. (1991) model. The model assumes a spherical potential with pure circular orbits, in which the observed radial velocity at a position (R, ψ) in the plane of the sky given by the relation:

$$v(R, \psi) = v_{\text{sys}}$$
$$+ \frac{A R \cos(\psi - \psi_0) \sin \theta \cos^p i}{\left\{ R^2 \left[\sin^2(\psi - \psi_0) + \cos^2(\psi - \psi_0) \right] + c_0^2 \cos^2 i \right\}^{p/2}},$$
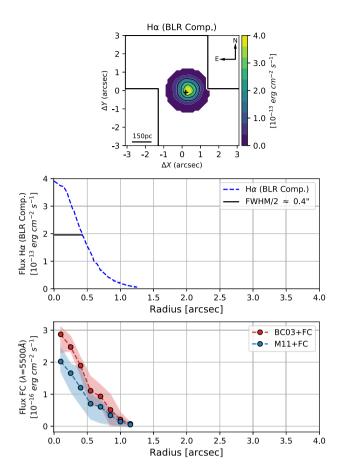$$(4)$$

where v_{sYs} is the systemic velocity, i the inclination of the disc (with $i = 0$ for a face-on disc), A is the amplitude of the curve, c_0 is the concentration parameter, and ψ_0 the line of nodes PA. The parameter p defines the form of the rotation curve, varying in the range between 1 (logarithm potential) and 1.5 (Keplerian potential). To avoid the degeneracy between the parameters, we restricted the disc inclination to have values of $i = 70 \pm 10$ (based on Duc et al. 2000, photometric analyses) and we assumed the kinematical centre to be co-spatial with the peak of the continuum emission. A Levenberg–Marquardt least-squares minimization was performed to determine the best fitting parameters and the uncertainties were obtained by making 100 Monte Carlo iterations. We show the best parameters and their uncertainties in Table 2.

The PA of the line of nodes was measured as $32 \pm 1°$, in agreement with previous values from the literature: PA $= 32°$ (Veilleux et al. 2001, hereafter V01), PA $= 30°$ (Marquez et al. 1998, hereafter

M98). V_{sYs} and i are also in reasonable agreement with other studies of the galaxy: V01 found, respectively, $2335 \pm 20 \text{ km s}^{-1}$ and $68°$, while M98 found 2330 km s^{-1} and $70°$. The velocity field amplitude ($A = 132 \pm 4 \text{ km s}^{-1}$), though, is much lower than the ones found by both V01 and M98 (225 ± 20 and 250 km s^{-1}). This discrepancy is probably due to the fact that both have used long-slit data in their studies, therefore being able to map the velocity field up to several kpc. Thus having a better constraint in the behaviour of the field at a larger radius, while our data can only recover the internal portion of the velocity field.

The modelled velocity field is shown in the middle right panel of Fig. 8, and the residuals between the observed field and model are shown in the bottom left panel of the same figure. The uncertainty map for the Component 1 v field, as measured by the Monte Carlo simulations described in the Section 4.1, is shown in the bottom right of Fig. 8. While most of the field is well represented by the disc rotation model ($|v - v_{MOdel}| < 20 \text{ km s}^{-1}$), there is one region at the eastern border with residuals up to 40 km s^{-1}. Since the maximum uncertainty in v is 15 km s^{-1}, this deviation from pure rotation is probably real. The same seems to be true for the σ field, shown in Fig. 9. The uncertainties in the Component 1 σ are of $\sim 5 \text{ km s}^{-1}$ in the central region, and up to 15 km s^{-1} at the borders, as shown in Fig. B1. Therefore, the lack of structure in the σ map is, in fact, real and not due to observational artefacts.[6]

---

[6]There is no clear evidence of the 'beam smearing' effect too, given that there is no increase in velocity dispersion values of Component1 in the central regions, where the gradient of the velocity field is maximum. The high values of velocity dispersion in Component 2, also cannot be purely due to this effect, because it is not co-spatial with the galactic centre and shows very blueshifted velocities from -250 to -200 km s^{-1}, as can be seen Fig. 9. Furthermore, when σ of both Component 2 and Component 1 are taken into account their values are in agreement with the ones measured from Brγ IR lines by Friedrich et al. (2010).
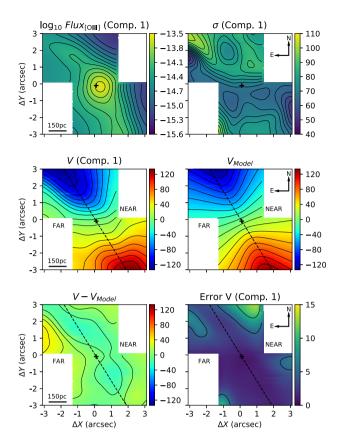
Figure 7. Top: Spatial distribution of the BLR component. Middle: Radial projection of the BLR component profile, vertical axis units of 10^{-13} erg s^{-1} cm^{-2}. Both show the point-like source emission of the BLR, with an FWHM ≈ 0.8 arcsec given by the spatial resolution of the observation. Bottom: Radial projection of the FC components fluxes (see Section 3), also presenting a point-like source emission.

These types of disturbances, in the both v and σ, are predicted by simulations (Kronberger et al. 2007; Bois et al. 2011) and observed (Torres-Flores et al. 2014; Hung et al. 2016; Bloom et al. 2018) in galaxies which are, or recently were, undergoing merging processes, as is the case of NGC 2992, and are attributed to perturbations in the gravitational potential due to tidal forces. In Paper II, we will investigate whether these disturbances are also present in the velocity field of NGC 2993.

The fainter component of the NLR (Component 2) is detected in a smaller region, originating near the continuum peak and extending towards the NW. For the brightest line, [O III]λ5007, the emission extends up to $\sim$3 arcsec, as shown by both the flux map, top left panel of Fig. 9 and the *P–V* plot in Fig. 10. In Fig. 9, we show the maps of equivalent width (EW) of [O III], σ and v for the Component 2. The v map shows only blueshifted velocities, with values ranging from -250 to -200 km s^{-1}. The velocity dispersion is higher than that of Component 1, ranging from 200 to 215 km s^{-1}. We also show in all the panels, the contours of the 8-shaped region detected in the 6 cm radio emission (in grey) in which the smaller loop seems to be co-spatial with Component 2.

The position–velocity plot along the major kinematical axis (PA $= 32°$) and the major axis of the radio emission (PA $= -26°$) of NGC 2992 are shown in Fig. 10. It is clear that while Component 1 has a rotational pattern, Component 2 deviates considerably from this pattern. Considering:

Figure 8. Component 1 properties. Top left: Log$_{10}$ flux [O III] λ5007 (erg s^{-1} cm^{-2}). Top right: Velocity dispersion σ (km s^{-1}). Middle left: Radial velocity v (km s^{-1}). Middle right: Modelled radial velocity (km s^{-1}), from the Bertola et al. (1991) rotation model fitting. Bottom left: Residual between the measured and the modelled velocity field. Bottom right: Uncertainties in the radial velocity v (km s^{-1}). Black cross is the continuum peak and the dashed black line is the fitted major axis PA.
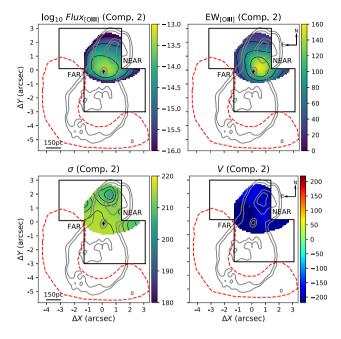
Table 2. Best fitting parameters Bertola et al. (1991) model.

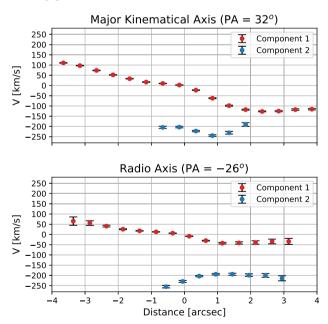| Parameters	Values
v_{sYs}	2345 ± 5 (km s^{-1})
A	132 ± 4 (km s^{-1})
p	1^a
c_0	3.5 ± 0.1 (arcsec)
ψ_0	$32° \pm 1°$
i	$70° \pm 1°$

Note. ^{a}In the model the parameters p is allowed to vary between 1 and 1.5, the fitted value was equals to 1 in all the Monte Carlo iterations.

(i) Component 2 is not following the galaxy's rotation;

(ii) it is co-spatial with the radio emission;

(iii) it has higher velocity dispersion values than those of Component 1, $\sigma > 200$ km s^{-1};

(iv) it has blueshifted velocities in the near side of the galaxy.

We are led to the conclusion that it is tracing a radio-jet driven gas outflow since all these are well-known characteristics of this type of phenomena. In fact, this ionized gas outflow was already reported by other IFU studies (e.g. García-Lorenzo et al. 2001; Friedrich et al. 2010; Mingozzi et al. 2019). Particularly, García-Lorenzo et al. (2001) interpreted this blueshifted structure as the interaction of
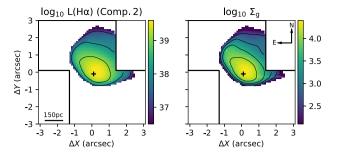
Figure 9. Component 2 properties. Top left: $\log_{10}$ flux [O III] $\lambda 5007$ (erg s^{-1} cm^{-2}). Top right: Equivalent width of [O III] $\lambda 5007$ (Å). Bottom left: Velocity dispersion, σ (km s^{-1}). Bottom right: Radial velocity, v (km s^{-1}). Solid black lines represent our FoV. Black cross is the continuum peak. Grey contours are the 6cm radio emission (Ulvestad & Wilson 1984). Red dashed line is the contour of the redshifted structure found by García-Lorenzo et al. (2001), at the farthest part of the radio emission major loop, taken from fig. 9 of their paper.

Figure 10. Position–velocity plot in virtual slits with 0.4 arcsec width. In the top panel, the slit is at the PA of the major kinematical axis, in the bottom the slit is at the PA of 8-shaped radio emission major axis. Points are the measured velocity values, and the error bars are the uncertainties in the velocities. Red points are the velocities of Component 1 and blue points the Component 2 ones.

the minor loop of the radio-jet with the interstellar medium (ISM). García-Lorenzo et al. (2001) also found a similar, however redshifted, structure in the far side of the galaxy, co-spatial with the farthest part of the radio emission major loop, which is mostly not visible in our

Figure 11. Left: Logarithm of Component 2 dereddened H α luminosity in erg s^{-1}. Right: Logarithm of Component 2 surface mass density in units of M$_\odot$ (0.1 arcsec)$^{-2}$. Black cross is the peak of the continuum emission.

FoV. We have extracted the contours of this structure from Fig. 9 of their paper and show it as the red dashed line in Fig. 9. This finding supports the scenario in which a bipolar overpressure relativistic plasma is expanding, accelerating, and compressing the ISM gas in its path (Chapman et al. 2000). Interestingly, the only portion of this structure that falls within our FoV is co-spatial with the largest velocity residuals seen in Fig. 8. Although our statistical analysis does not indicate the necessity of a separate component, the large residuals clearly indicate a perturbation in the velocity field.

A very similar geometry was found by Riffel & Storchi-Bergmann (2011) in the galaxy Mrk 1157, in which non-rotational blueshifted and redshifted structures are present and co-spatial to the two loops of a very similar nuclear 8-shaped radio emission. The authors also interpreted these structures as the effect of the expanding radio-emitting gas into the ionized ISM.

4.3 Outflow properties

If we consider Component 2 as ionized outflowing gas, we can measure its properties such as mass, mass outflow rate and kinetic power. We followed the prescriptions described in Lena et al. (2015), in which a biconical outflow geometry is assumed, even though in our case we can see only one of the cones.

The mass outflow rate can be estimated as the ratio between the mass of the outflowing gas and the dynamical time (time for the gas to reach the present distance from the nucleus), M_g/t_d. The mass of the gas in outflow (Component 2) is estimated as

$$M_g = n_e m_p V f \tag{5}$$

where m_p is the proton mass, n_e and V are the electron density and the volume of the region where the component is detected, f is the filling factor. The filling factor and volume are eliminated by combining equation (5) with the following expression for the H α luminosity:

$$L(\text{H}\alpha) \approx f n_e^2 j_{\text{H}\alpha} V \tag{6}$$

with $j_{\text{H}\alpha} = 3.534 \times 10^{-25}$ erg cm^3 s^{-1} at $T = 10\,000$ K (Osterbrock & Ferland 2006). Therefore, the gas mass can be written as

$$M_g = \frac{m_p L(\text{H}\alpha)}{n_e j_{\text{H}\alpha}}. \tag{7}$$

Our estimates for n_e are based on the flux ratio between [S II] lines, as described in Appendix C. Please note the $L(\text{H}\alpha)$ used here is based on the flux of Component 2 H α emission only, corrected by extinction as described in Appendix C. The spatially resolved $L(\text{H}\alpha)$ and M_g (i.e. gas mass surface density, Σ_g) are shown in Fig. 11.

The integrated gas mass is $M_g = 3.6 \pm 0.6 \times 10^6$ M$_\odot$. The t_d was estimated as the ratio between the maximum extension of the outflow ~ 3 arcsec ≈ 450 pc (see Fig. 10) to its mean velocity,

$\langle v_{Out} \rangle \approx 210$ km s^{-1}, which gives $t_d \approx 2.2 \times 10^6$ yr. Combining these values we estimated an outflow mass rate of $\dot{M}_{out} \approx 1.6 \pm 0.6$ M$_\odot$.

We also estimated the outflow kinetic power as

$$\dot{E}_{out} = \frac{\dot{M}_{out} v_{out}^2}{2}, \qquad (8)$$

where v_{Out} is the radial velocity of Component 2 (Fig. 9). Integrating the entire outflow we obtained a total outflow kinetic power $\dot{E}_{out} \approx 2.2 \pm 0.3 \times 10^{40}$ erg s^{-1}. In Section 6.3, we compare these values with the ones found in the literature and those expected by outflow–AGN relations.

5 IONIZATION MECHANISMS

Given the presence of young stars discussed in Section 3, X-ray (Section 1) and BLR emission (Section 4) that indicate AGN excitation, and the presence of radio emission that can drive shocks (Dopita 2002; Allen et al. 2008), we used the [N II]/Hα versus [O III]/Hβ and [S II]/Hα versus [O III]/Hβ (Baldwin, Phillips & Terlevich 1981, BPT) diagnostic diagrams to investigate which of these excitation mechanisms are dominant in the innermost region of the galaxy.

In the bottom panels of Fig. 12, we show the maps of [O III]/Hβ, [N II]/Hα, and [S II]/Hα line ratios for the entire line profile (by summing the kinematical components; we do that to increase the precision in the flux measurement and to avoid regions where a second component is detected in high S/N lines, like [O III], but not detected in lower S/N ones, like Hβ). We excluded the regions where uncertainties in the total flux, as shown in Appendix B, are higher than 30 per cent. The [O III]/Hβ shows a clear AGN signature, with its peak, up to [O III]/H$\beta \approx 25$, at the centre of the FoV and decreasing radially down to [O III]/H$\beta \approx 2$ at SW corner of the FoV. The [N II]/Hα and [S II]/Hα, however, do not show the same pattern: their maximum values are off-nuclear, and they do not present a radial decrease as in the [O III]/Hβ one. This indicates a lower energy mechanism (lower than an AGN, but higher than H II regions) can be ionizing the gas too. In fact, shock ionized regions are characterized by having smaller [O III]/Hβ ratios and larger [S II]([N II])/Hα than those ionized by AGNs (Veilleux & Osterbrock 1987; Kewley et al. 2006; Allen et al. 2008).

We selected limiting regions in the line ratio maps and shown it in the respectively BPT diagrams in the top panels of Fig. 12. We also show some division lines: the solid black curves on both diagnostic diagrams trace the Kewley et al. (2001) theoretical upper limit of regions ionized by pure star formation (K01 line). All spectra lying above the K01 line are dominated by ionization mechanisms more energetic than star formation. Several excitation mechanisms can increase the collisional excitation rate, enhancing the ratios of the forbidden to recombination lines, among them energetic photons from a power law-like emission (AGN); shock excitation and evolved stellar populations (pos-AGB) can also produce line ratios along this branch of the diagram. The latter case does not apply to the nuclear region of NGC 2992 given that it requires EW(Hα) < 3 Å (Stasinska et al. 2008; Cid Fernandes et al. 2011) and our entire FoV has EW(Hα) > 10 Å. We also show the dashed black curve on the [N II]/Hα versus [O III]/Hβ diagnostic diagram: the Kauffmann et al. (2003) empirical classification line (Ka03 line), which traces the upper boundary of the Sloan Digital Sky Survey Strauss et al. (SDSS 2002) star formation sequence. All spectra lying below the Ka03 line are dominated by star formation. The dash–dotted black curve on the [S II]/Hα versus [O III]/Hβ diagnostic diagram traces the Kewley

et al. (2006) empirical classification line (K06 line), which separates high-ionization spectra associated with Seyfert (AGN) and other intermediary ionization mechanisms including shock excitation. We also show as grey points in the top BPT diagrams a collection of single-fibre emission line measurement from SDSS main galaxy sample by Kewley et al. (2006).

Region A is the peak of the [O III]/Hβ map, it shows clear AGN-like ratios, with an upper [O III]/Hβ value higher than any SDSS AGN, which corresponds to a 3 arcsec diameter aperture, and therefore has a diluted AGN/host-galaxy emission line ratio. Region B has the lowest value in all the maps; it lies below K01, showing the radial decrease in the AGN contribution to the emission lines and significant contributions from both star formation and AGN excitation. Regions C, D, and E display the highest values in the [S II]/Hα and [N II]/Hα maps; however, they have lower [O III]/Hβ values than region A. Region E, in fact, crosses the K06 line in the [S II]/Hα diagram, which again indicates the presence of another ionization mechanism.
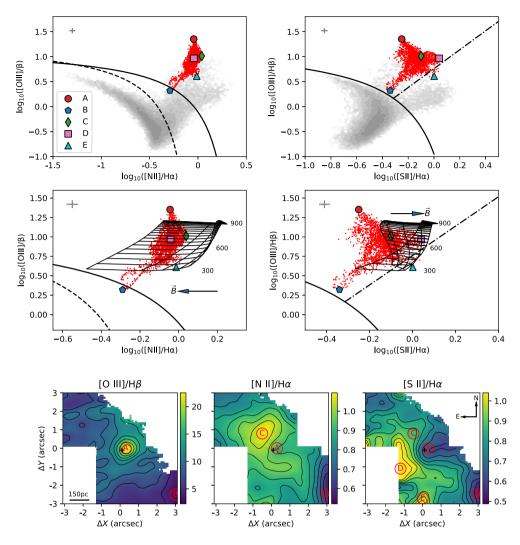
In order to search for an explanation to the increase in this intermediary ionization energy lines ([N II] and [S II]) we used the MAPPINGS V shock models by Sutherland et al. (2018). We explored the parameter space in the pure shock and shock + precursor grids of the models. None of the pure shock models could explain these line ratios, given the high [O III]/Hβ values. However shock + precursor (Shock ionization in a medium already ionized by power-law-like emission) with shock velocities between 300 and 900 km s^{-1} and magnetic field ($\vec{B}$) between 0.01 and 4 μG, with a two-solar metallicity and a pre-shock density of 1 cm^{-3}, successfully reproduce the line ratios of regions C, D, and E. In the middle panels of Fig. 12, we show the grid models in these shock velocity and magnetic field ranges superimposed with the emission line ratios of the regions. The shocks in NGC 2992 have been extensively studied by Allen et al. (1999), who conclude that shocks are the predominant ionization mechanism in the extended NLR cones at a distance of several kpc from the nucleus.

We can conclude that a more simple Starburst–AGN mixture (e.g. Davies et al. 2014a,b; D'Agostino et al. 2018) in which the maximum values of all [O III]/Hβ, [N II]/Hα, and [S II]/Hα are located in the innermost spaxel (location of the AGN), and all decrease radially towards the H II ionization region of the BPT in a straight line (see for example fig. 1 in Davies et al. 2014b), cannot describe the ionization at the circumnuclear region of NGC 2992. Instead, a more complex Starburst–AGN–Shocks mixture is responsible for its ionization. However, the very high values of [O III]/Hβ indicate the most important among these three mechanisms is AGN ionization, at least in the innermost portion (see further discussion in Section 6.4).

6 DISCUSSION

6.1 Interaction-driven circumnuclear star formation

In general terms, the stellar population synthesis discussed in Section 3 shows that stellar content in the inner 1.1 kpc of NGC 2992 is mainly composed by an old metal-rich population, with a smaller but considerable contribution from young metal-poor stars. The presence of the latter is supported by other studies, for instance, using the Bica & Alloin (1986) base of star clusters for stellar population synthesis, Storchi Bergmann, Bica & Pastoriza (1990) found a predominance of old stellar populations (10^{10} yr) and a small contribution of at least 5 per cent by recent star formation in the inner 5 arcsec. Moreover, Friedrich et al. (2010) find that 10–20 per cent of the IR flux is attributable to a starburst, based on the emission from polycyclic

Figure 12. Top: [N II]/Hα versus [O III]/Hβ and [S II]/Hα versus [O III]/Hβ BPT diagrams; grey contours are galaxies from the SDSS main galaxy sample measured by Kewley et al. (2006). red points are the spaxel of NGC 2992. Coloured markers are the selected regions of NGC 2992, as shown in the bottom panels, representing: red (Region A), blue (B), green (C), pink (D), and cyan (E). Middle: Zoomed BPT diagrams with shock + precursor grid models as measured with MAPPINGS V code (Sutherland et al. 2018); the $\vec{B}$ indicates increasing magnetic field of the model (from 0.01 to 4 μG); the black numbers indicate the velocities of the shocks, ranging from 300 to 900 km s^{-1}. Bottom: Respectively, from left to right, [O III]/Hβ, [N II]/Hα, and [S II]/Hα emission lines ratio maps; red circles show the selected regions shown in the upper panels. In BPT diagrams, the grey crosses are the typical errors in the emission line ratios; the solid black lines are Kewley et al. (2001) theoretical upper limits for pure star forming galaxies. In the [N II]/Hα versus [O III]/Hβ diagram the dashed black line represents Kauffmann et al. (2003) line which traces the upper boundary of the SDSS star formation sequence. In the [S II]/Hα versus [O III]/Hβ diagram the dash–dotted black line represents the empirical division between AGN-like and low-ionization nuclear emission-line region (LINER) (Kewley et al. 2006).

aromatic hydrocarbon (PAH) molecules. Additionally, these authors estimate the starburst to have occurred between 40 and 50 Myr, based on the equivalent width of the Br γ line.

Major merger processes are known to be responsible for gas inflow towards the central regions of galaxies enhancing circumnuclear star formation and possibly triggering nuclear activity. Merger galaxies have an increase in the SFR, mainly at the nuclear regions (Ellison et al. 2013; Pan et al. 2019). Thus, these sources have younger nuclear populations than those found in isolated galaxies, in which most of their recent formed stars are concentrated at the spiral arms. Moreover, major mergers are also able to modify the metallicity gradients of galaxies (Barrera-Ballesteros et al. 2015). Galaxy simulations show that the gas, originally located at external portions of the isolated galaxy (metal-poor regions), moves towards internal regions (metal-rich regions) of the companion galaxy during the encounter and is capable of cooling and forming stars.. Such processes are able

to explain both the increase in the SFR and the modifications in the metallicity gradient (Dalcanton 2007; Torrey et al. 2012; Sillero et al. 2017). In fact, the pericentre passage between NGC 2992 and its companion NGC 2993 is estimated to have occurred ∼100 Myr ago (Duc et al. 2000). Thus, a possible scenario is that metal-poor gas inflow has led to interaction-driven circumnuclear star formation which can explain the presence of such young metal-poor stellar population in the nucleus. Such inflows could also be responsible for triggering NGC 2992's nuclear activity, a scenario which will be further explored using numerical simulations in Paper III.

6.2 Feeding versus feedback

We can compare the mass outflow rate, estimated in Section 4.3, with the accretion rate necessary to power the AGN at the nucleus of

NGC 2992, calculated as follows:

$$\dot{M}_{\rm BH} = \frac{L_{\rm bol}}{c^2 \eta}, \qquad (9)$$

where η is the mass–energy conversion efficiency, which for Seyfert galaxies is usually assumed to be $\eta = 0.1$ (Frank, King & Raine 2002), $L_{\rm bol}$ is the bolometric luminosity of the AGN, and c is the speed of light. To measure $L_{\rm bol}$, we applied the bolometric correction by Marconi et al. (2004) on the most recent X-ray luminosity measurement of NGC 2992 made by Marinucci et al. (2018). The author used a 2015 *NuSTAR* observation and obtained an absorption corrected 2–10 kev luminosity of $7.6 \pm 0.1 \times 10^{42}$ ergs^{-1} that translates to $L_{bol} = 9.1 \pm 0.2 \times 10^{43}$ ergs^{-1}. We use these values to derive an accretion rate of $\dot{M}_{\rm BH} \approx 0.02$ M$_\odot$ yr^{-1}.

The nuclear accretion rate is two orders of magnitude smaller than the mass outflow rate ($\dot{M}_{\rm out} \approx 1.6 \pm 0.6$ M$_\odot$ yr^{-1}, see Section 4.3). This implies that most of the outflowing gas does not originate in the AGN, but in the surrounding ISM, and this result supports the scenario in which the plasma bubbles (radio loops) are expanding, pushing gas away from the nuclear region. However, the ratio between the kinetic power of this blueshifted outflow loop and the bolometric luminosity is ~ 0.002, which means only 0.2 per cent of the AGN radiative power is in this outflow. Many authors argue that such a low value is not enough to have the feedback effects expected by cosmological simulations (Springel et al. 2005; Silk & Mamon 2012; Bullock & Boylan-Kolchin 2017), stating that $\dot{E}_{\rm out}/L_{bOl}$ should be closer to 5 per cent or above in order to effectively suppress growth in the most massive galaxies. However, some models show that coupling efficiencies of $\dot{E}_{\rm out}/L_{bOl} \approx 0.5$ per cent (Hopkins & Elvis 2010), and even 0.1 per cent (Costa et al. 2018) could successfully prevent star formation.

6.3 AGN–wind scaling relations

Comparing our outflow measurements with those from the literature we noted ours results disagree with those presented in Müller-Sánchez et al. (2011), who reported $\dot{M}_{\rm out}= 120$ M$_\odot$ yr^{-1} and $\dot{E}_{\rm out} = 2.5 \times 10^{42}$ erg s^{-1}, both almost 100 times greater than ours. We attribute this difference to two factors: (i) they assumed the filling factor f to be constant equal to 0.001, while we have measured the filling factor from $L(\text{H}\alpha)$ and n_e (see equation 6). This assumption makes their M_g proportional to n_e, and not inversely proportional (as in equation 7); (ii) they assume an electronic density of $n_e = 5000$ cm^{-3}, a value more than five times larger than the maximum value we measured in the nuclear region of the galaxy. These two factors combined explain their overestimation of both $\dot{M}_{\rm out}$ and $\dot{E}_{\rm out}$. We also argue these differences cannot be due to a larger coverage of the outflow by a larger field of view, in the sense of seeing the farthest part of the radio emission major loop and its redshifted outflow structure, given the authors have used the OSIRIS/VLT instrument, which has an even smaller FoV than GMOS.

We can compare our values to the properties of outflows found in other precious papers across the literature. In Fig. 11, we show the Fiore et al. (2017) compilation of a set of outflow energetics from various studies over the years spanning a large range of AGN luminosity ($L_{bOl} \geq 10^{44}$), which they use to establish AGN wind scaling relations, mass outflow rate, and outflow power as a function of bolometric luminosity, together with several measurements of nearby galaxies from individual studies compiled by us from the literature or obtained by our collaborators: NGC 1068, NGC 3783, NGC 6814, NGC 7469 (Müller-Sánchez et al. 2011), NGC 4151 (Crenshaw et al. 2015), Mrk 573 (Revalski et al. 2018), Mrk 34 (Revalski et al. 2018),

NGC 7582 (Riffel et al. 2009), Mrk 1066 (Riffel, Storchi-Bergmann & Nagar 2010b), Mrk 1157 (Riffel & Storchi-Bergmann 2011), Mrk 79 (Riffel, Storchi-Bergmann & Winge 2013a), NGC 5929 (Riffel, Storchi-Bergmann & Riffel 2013b), NGC 5728 (Shimizu et al. 2019), and NGC 3081 (Schnorr-Müller et al. 2014), ESO 362-G18 (Humire et al. 2018), NGC 1386 (Lena et al. 2015), ESO 153-G20 (Soto-Pinto et al. 2019), 3C 33 (Couto, Storchi-Bergmann & Schnorr-Müller 2017), including NGC 2992 measurement by Müller-Sánchez et al. (2011). Although these estimates are made using different recipes, leading to differences between methods, they are generally similar to the one adopted here. Therefore, this comparison with the literature may be useful at least as an order of magnitude approximation.

As we can see, the overestimated previous measurement of NGC 2992's outflow made this source to be an outlier in the Fiore et al. (2017) relations, while our values make the galaxy more likely to be explained by these relations. However, the other measurements in nearby Seyfert galaxies support the existence of a larger scatter of these relations, both in $\dot{E}_{\rm out}$ and $\dot{M}_{\rm out}$, at lower luminosities. To confirm whether this extension is valid or not, more detailed studies like this, mainly using IFU, are needed so that outflow properties can be properly and systematically measured, without assuming fixed values of n_e and f.
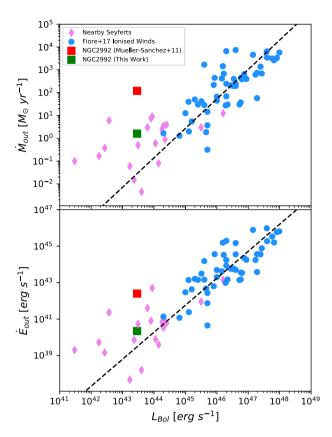
6.4 Multiple ionization mechanisms

In Section 5, we showed that despite being dominated by AGN excitation, star formation, and shocks cannot be excluded as ionization mechanisms in the nuclear region of the galaxy. The existence of star formation ionization in the nucleus is confirmed by Friedrich et al. (2010) IR emission line analyses, as mentioned in Section 6.1. The presence of shocks is also supported by Allen et al. (1999) using long-slit spectroscopy. The authors also argue the dominance of shocks increases, compared to ionization by the central source, at larger radius.

Galaxies undergoing rapid phases of evolution (through processes such as galaxy–galaxy interactions, gas outflows and radio jets) often have multiple ionization mechanisms contributing to their optical line emission (e.g. Rich, Kewley & Dopita 2011; Lanz et al. 2015; Rich, Kewley & Dopita 2015; Davies et al. 2017). These multiple ionization mechanisms are also in agreement with evolutionary scenarios in which gas inflows (driven either by secular mechanisms, like nuclear bars or nuclear spiral arms, or environmental ones, like minor and major mergers) triggers nuclear star formation and nuclear activity (feeding process) and then the active nucleus can drive both ionizing photons from the accretion disc and radio jets (feedback process) that impacts the ISM physical conditions (Hopkins et al. 2008; Hopkins & Quataert 2010).

7 SUMMARY AND CONCLUSIONS

We have analysed the stellar population, the ionization mechanism, and kinematics of the ionized gas in the inner 1.1 kpc of the interacting Seyfert galaxy NGC 2992, using optical spectra obtained with the GMOS integral field spectrograph on the Gemini South telescope, with a spatial resolution of $\approx$120 pc and spectral resolution $\approx$40 km s^{-1}. The main results are as follows:

(i) The stellar population in the nuclear region of the galaxy is mainly composed (60 per cent $\leq x_O \leq$ 80 per cent) by an old ($t > 1.4$ Gyr) metal-rich ($\langle Z \rangle_O \geq 2.0$ Z$_\odot$) population with a smaller, but considerable contribution (10 per cent $\leq x_Y \leq$ 30 per cent) of

Figure 13. Correlations between the mass outflow rate ($\dot{M}_{\rm out}$, top panel) and kinetic outflow power ($\dot{E}_{\rm out}$, bottom panel). Blue points are the data compiled by Fiore et al. (2017) and the black dashed lines show the best-fitting correlations for these points. Red squares are the previous measurement of NGC 2992 by Müller-Sánchez et al. (2011), and green ones are the results of this work. Violet diamonds are compiled from various literature sources for more modest AGN luminosities.

an young ($t < 100$ Myr) metal-poor ($\langle Z \rangle_Y \leq 1.0\ Z_\odot$) population. A possible scenario is that metal-poor gas inflow during the pericentre passage of NGC 2993 has led to interaction-driven circumnuclear star formation, which can explain the presence of such young metal-poor stellar population in the nuclear region.

(ii) The emission line analyses show the presence of both BLR and NLR emission, confirming its classification as an intermediate-type Seyfert galaxy. The BLR emission profile has a velocity dispersion of $\rm FWHM_{BLR} = 2010\ km\ s^{-1}$ and a Balmer decrement of $(\rm H\alpha/H\beta)_{BLR} = 24.2$. The NLR presents two distinctly kinematical components: one that although disturbed is well fitted by a disc model, and therefore can be identified as gas in orbit in the galaxy disc, with radial velocities ranging from -130 to $130\ \rm km\ s^{-1}$; another that we interpreted as an outflow associated with the radio emission, with blueshifted velocities of $\sim 200\ \rm km\ s^{-1}$, a mass outflow rate of $\dot{M}_{out} \approx 1.6 \pm 0.6\ M_\odot$ and a kinematic power of $\dot{E}_{out} \approx 2.2 \pm 0.3 \times 10^{40}\ \rm erg\ s^{-1}$.

(iii) The BPT diagnostic diagrams show the galaxy possess multiple ionization mechanisms: a mixture of AGN, star formation, and shocks, the former being the dominant one. The [O III]/Hβ ratio peaks at the innermost spaxels, and is located in the upper region of the BPT diagram. The lower values, located at the border of the FoV, decreases down to below the Kewley et al. (2001) line, showing an increase in the star formation ionization compared to the AGN ionization at larger radius. Off-nuclear peaks in the [N II]/Hα and [S II]/Hα maps indicate the presence of another mechanism and are

successfully explained by Sutherland et al. (2018) shock + precursor models.

DATA AVAILABILITY

The data underlying this article will be shared on reasonable request to the corresponding author.

REFERENCES

Allen M. G., Dopita M. A., Tsvetanov Z. I., Sutherland R. S., 1999, ApJ, 511, 686
Allen M. G., Groves B. A., Dopita M. A., Sutherland R. S., Kewley L. J., 2008, ApJS, 178, 20
Alloin D., Collin-Souffrin S., Joly M., Vigroux L., 1979, A&A, 78, 200
Bacon R. et al., 2010, in McLean I. S., Ramsay S. K., Takami H., eds, Proc. SPIE Conf. Ser. Vol. 7735, Ground-Based and Airborne Instrumentation for Astronomy III. SPIE, Bellingham, p. 773508
Baldwin J. A., Phillips M. M., Terlevich R., 1981, PASP, 93, 5
Baldwin C., McDermid R. M., Kuntschner H., Maraston C., Conroy C., 2018, MNRAS, 473, 4698
Barrera-Ballesteros J. K. et al., 2015, A&A, 579, A45
Begelman M. C., Blandford R. D., Rees M. J., 1984, Rev. Mod. Phys., 56, 255
Bennert N., Jungwiert B., Komossa S., Haas M., Chini R., 2006, A&A, 456, 953
Bertola F., Bettoni D., Danziger J., Sadler E., Sparke L., de Zeeuw T., 1991, ApJ, 373, 369
Bica E., Alloin D., 1986, A&A, 162, 21
Block A., 2011, Caelum-Observatory: NGC 2992, http://www.caelumobservatory.com/gallery/n2992.shtml
Bloom J. V. et al., 2018, MNRAS, 476, 2339
Blumenthal K. A., Barnes J. E., 2018, MNRAS, 479, 3952
Bois M. et al., 2011, MNRAS, 416, 1654
Bruzual G., Charlot S., 2003, MNRAS, 344, 1000
Bullock J. S., Boylan-Kolchin M., 2017, ARA&A, 55, 343
Calzetti D., Armus L., Bohlin R. C., Kinney A. L., Koornneef J., Storchi-Bergmann T., 2000, ApJ, 533, 682
Cappellari M., Copin Y., 2003, MNRAS, 342, 345
Cardelli J. A., Clayton G. C., Mathis J. S., 1989, ApJ, 345, 245
Cardoso L. S. M., Gomes J. M., Papaderos P., 2017, A&A, 604, A99
Chabrier G., 2003, PASP, 115, 763
Chapman S. C., Morris S. L., Alonso-Herrero A., Falcke H., 2000, MNRAS, 314, 263

Chen X. Y., Liang Y. C., Hammer F., Prugniel P., Zhong G. H., Rodrigues M., Zhao Y. H., Flores H., 2010, A&A, 515, A101

Cid Fernandes R. et al., 2013, A&A, 557, A86

Cid Fernandes R., 2018, MNRAS, 480, 4480

Cid Fernandes R., González Delgado R. M., 2010, MNRAS, 403, 780

Cid Fernandes R., Gu Q., Melnick J., Terlevich E., Terlevich R., Kunth D., Rodrigues Lacerda R., Joguet B., 2004, MNRAS, 355, 273

Cid Fernandes R., Mateus A., Sodré L., Stasińska G., Gomes J. M., 2005, MNRAS, 358, 363

Cid Fernandes R., Stasinska G., Mateus A., Vale Asari N., 2011, MNRAS, 413, 1687

Colina L., Fricke K. J., Kollatschny W., Perryman M. A. C., 1987, A&A, 178, 51

Conroy C., 2013, Annu. Rev. Astron. Astrophys., 51, 393

Costa T., Rosdahl J., Sijacki D., Haehnelt M. G., 2018, MNRAS, 479, 2079

Couto G. S., Storchi-Bergmann T., Schnorr-Müller A., 2017, MNRAS, 469, 1573

Crenshaw D. M., Fischer T. C., Kraemer S. B., Schmitt H. R., 2015, ApJ, 799, 83

Croton D. J. et al., 2006, MNRAS, 365, 11

D'Agostino J. J., Poetrodjojo H., Ho I.-T., Groves B., Kewley L., Madore B. F., Rich J., Seibert M., 2018, MNRAS, 479, 4907

Dalcanton J. J., 2007, ApJ, 658, 941

Dametto N. Z. et al., 2019, MNRAS, 482, 4437

Davies R. L. et al., 2017, MNRAS, 470, 4974

Davies R. L., Rich J. A., Kewley L. J., Dopita M. A., 2014a, MNRAS, 439, 3835

Davies R. L., Kewley L. J., Ho I. T., Dopita M. A., 2014b, MNRAS, 444, 3961

Di Matteo T., Springel V., Hernquist L., 2005, Nature, 433, 604

Dopita M. A., 2002, in Henney W. J., Steffen W., Binette L., Raga A., eds, Revista Mexicana de Astronomia y Astrofisica Conference Series Vol. 13, México. p. 177

Duc P.-A., Brinks E., Springel V., Pichardo B., Weilbacher P., Mirabel I. F., 2000, AJ, 120, 1238

Ellison S. L., Patton D. R., Mendel J. T., Scudder J. M., 2011, MNRAS, 418, 2043

Ellison S. L., Mendel J. T., Patton D. R., Scudder J. M., 2013, MNRAS, 435, 3627

Event Horizon Telescope Collaboration, 2019, ApJ, 875, L1

Fan L. et al., 2016, ApJ, 822, L32

Ferrarese L., Merritt D., 2000, ApJ, 539, L9

Ferré-Mateu A., Vazdekis A., Trujillo I., Sánchez-Blázquez P., Ricciardelli E., de la Rosa I. G., 2012, MNRAS, 423, 632

Fiore F. et al., 2017, A&A, 601, A143

Fischer T. C. et al., 2018, ApJ, 856, 102

Frank J., King A., Raine D. J., 2002, Accretion Power in Astrophysics, 3rd edn, Cambridge University Press, Cambridge

Freund J., 1992, Annalen Der Physik – Annals of Physics, 504, 380

Friedrich S., Davies R. I., Hicks E. K. S., Engel H., Müller-Sánchez F., Genzel R., Tacconi L. J., 2010, A&A, 519, A79

García-Bernete I. et al., 2015, MNRAS, 449, 1309

García-Lorenzo B., Arribas S., Mediavilla E., 2001, A&A, 378, 787

Ge J., Mao S., Lu Y., Cappellari M., Yan R., 2019, MNRAS, 485, 1675

Gilli R., Maiolino R., Marconi A., Risaliti G., Dadina M., Weaver K. A., Colbert E. J. M., 2000, A&A, 355, 485

Glikman E., Simmons B., Mailly M., Schawinski K., Urry C. M., Lacy M., 2015, ApJ, 806, 218

González Delgado R. M. et al., 2015, A&A, 581, A103

Greene J. E., Zakamska N. L., Smith P. S., 2012, ApJ, 746, 86

Hopkins P. F., Elvis M., 2010, MNRAS, 401, 7

Hopkins P. F., Quataert E., 2010, MNRAS, 407, 1529

Hopkins P. F., Hernquist L., Cox T. J., Kereš D., 2008, ApJS, 175, 356

Humire P. K. et al., 2018, A&A, 614, A94

Hung C.-L., Hayward C. C., Smith H. A., Ashby M. L. N., Lanz L., Martínez-Galarza J. R., Sanders D. B., Zezas A., 2016, ApJ, 816, 99

Irwin J. A. et al., 2017, MNRAS, 464, 1333

Kauffmann G. et al., 2003, MNRAS, 346, 1055

Kennicutt Robert C. J., 1998, ApJ, 498, 541

Kewley L. J., Dopita M. A., Sutherland R. S., Heisler C. A., Trevena J., 2001, ApJ, 556, 121

Kewley L. J., Groves B., Kauffmann G., Heckman T., 2006, MNRAS, 372, 961

Koleva M., Prugniel P., Ocvirk P., Le Borgne D., Soubiran C., 2008, MNRAS, 385, 1998

Kormendy J., Ho L. C., 2013, ARA&A, 51, 511

Koski A. T., 1978, ApJ, 223, 56

Koss M., Mushotzky R., Veilleux S., Winter L., 2010, ApJ, 716, L125

Kronberger T., Kapferer W., Schindler S., Ziegler B. L., 2007, A&A, 473, 761

Trippe L. M., Crenshaw D. R. P. D., Dietrich M., 2008, AJ, 135, 2048

Lanz L., Ogle P. M., Evans D., Appleton P. N., Guillard P., Emonts B., 2015, ApJ, 801, 17

Le Borgne J.-F. et al., 2003, A&A, 402, 433

Lena D. et al., 2015, ApJ, 806, 84

Madau P., Dickinson M., 2014, ARA&A, 52, 415

Maksym W. P., Ulmer M. P., Roth K. C., Irwin J. A., Dupke R., Ho L. C., Keel W. C., Adami C., 2014, MNRAS, 444, 866

Mallmann N. D. et al., 2018, MNRAS, 478, 5491

Maraston C., Strömbäck G., 2011, MNRAS, 418, 2785

Marconi A., Risaliti G., Gilli R., Hunt L. K., Maiolino R., Salvati M., 2004, MNRAS, 351, 169

Marinucci A., Bianchi S., Braito V., Matt G., Nardini E., Reeves J., 2018, MNRAS, 478, 5638

Marquez I., Boisson C., Durret F., Petitjean P., 1998, A&A, 333, 459

McElroy R., Croom S. M., Pracy M., Sharp R., Ho I. T., Medling A. M., 2015, MNRAS, 446, 2186

Menci N., Gatti M., Fiore F., Lamastra A., 2014, A&A, 569, A37

Menezes R. B., Steiner J. E., Ricci T. V., 2014, MNRAS, 438, 2597

Mentz J. J. et al., 2016, MNRAS, 463, 2819

Mingozzi M. et al., 2019, A&A, 622, A146

Müller-Sánchez F., Prieto M. A., Hicks E. K. S., Vives-Arias H., Davies R. I., Malkan M., Tacconi L. J., Genzel R., 2011, ApJ, 739, 69

Osterbrock D. E., Ferland G. J., 2006, in Sausalito C., ed., Astrophysics of Gaseous Nebulae and Active Galactic Nuclei, University Science Books

Pan H.-A. et al., 2019, ApJ, 881, 119

Peterson B. M., 1997, An Introduction to Active Galactic Nuclei, Cambridge University Press

Peterson B. M., Wanders I., Bertram R., Hunley J. F., Pogge R. W., Wagner R. M., 1998, ApJ, 501, 82

Pettini M., Pagel B. E. J., 2004, MNRAS, 348, L59

Proxauf B., Öttl S., Kimeswenger S., 2014, A&A, 561, A10

Raimann D., Storchi-Bergmann T., González Delgado R. M., Cid Fernandes R., Heckman T., Leitherer C., Schmitt H., 2003, MNRAS, 339, 772

Revalski M., Crenshaw D. M., Kraemer S. B., Fischer T. C., Schmitt H. R., Machuca C., 2018, ApJ, 856, 46

Rich J. A., Kewley L. J., Dopita M. A., 2011, ApJ, 734, 87

Rich J. A., Kewley L. J., Dopita M. A., 2015, ApJS, 221, 28

Riffel R. A., Storchi-Bergmann T., 2011, MNRAS, 417, 2752

Riffel R. A., Storchi-Bergmann T., Dors O. L., Winge C., 2009, MNRAS, 393, 783

Riffel R., Pastoriza M. G., Rodríguez-Ardila A., Bonatto C., 2010, in Bruzual G. R., Charlot S., eds, IAU Symp. 262, Stellar Populations – Planning for the Next Decade, Cambridge University Press, Cambridge, UK, p. 164

Riffel R. A., Storchi-Bergmann T., Nagar N. M., 2010b, MNRAS, 404, 166

Riffel R. A., Storchi-Bergmann T., Winge C., 2013a, MNRAS, 430, 2249

Riffel R. A., Storchi-Bergmann T., Riffel R., 2013b, ApJ, 780, L24

Rupke D. S. N., Veilleux S., 2011, ApJ, 729, L27

Ruschel-Dutra D., 2020, danielrd6/ifscube v1.0

Sánchez-Blázquez P. et al., 2006, MNRAS, 371, 703

Satyapal S., Ellison S. L., McAlpine W., Hickox R. C., Patton D. R., Mendel J. T., 2014, MNRAS, 441, 1297

Schawinski K., Dowlin N., Thomas D., Urry C. M., Edmondson E., 2010, ApJ, 714, L108

Schimoia J. S., Storchi-Bergmann T., Grupe D., Eracleous M., Peterson B. M., Baldwin J. A., Nemmen R. S., Winge C., 2015, ApJ, 800, 63

Schlafly E. F., Finkbeiner D. P., 2011, ApJ, 737, 103

Schnorr-Müller A. et al., 2016, MNRAS, 462, 3570

Schnorr-Müller A., Storchi-Bergmann T., Nagar N. M., Robinson A., Lena D., Riffel R. A., Couto G. S., 2014, MNRAS, 437, 1708

Schnorr-Müller A., Storchi-Bergmann T., Nagar N. M., Robinson A., Lena D., 2017, MNRAS, 471, 3888

Shimizu T. T. et al., 2019, MNRAS, 490, 5860

Shuder J. M., 1980, ApJ, 240, 32

Silk J., Mamon G. A., 2012, Res. Astron. Astrophys., 12, 917

Sillero E., Tissera P. B., Lambas D. G., Michel-Dansac L., 2017, MNRAS, 472, 4404

Silverman J. D. et al., 2008, ApJ, 679, 118

Soto-Pinto P. et al., 2019, MNRAS, 489, 4111

Springel V. et al., 2005, Nature, 435, 629

Stasinska G., Asari N. V., Fernandes R. C., Gomes J. M., Schlickmann M., Mateus A., Schoenell W., Sodré L., Jr, 2008, MNRAS, 391, L31

Storchi Bergmann T., Bica E., Pastoriza M. G., 1990, MNRAS, 245, 749

Storchi-Bergmann T. et al., 2018, ApJ, 868, 14

Storchi-Bergmann T., Raimann D. I., González Delgado R. M., Schmitt H. R., Cid Fernandes R., Heckman T., Leitherer C., 2003, in Perez E., Gonzalez Delgado R. M., Tenorio-Tagle G., eds, ASP Conf. Ser. Vol. 297, Star Formation Through Time. Astron. Soc. Pac., San Francisco, p. 363

Strauss M. A. et al., 2002, AJ, 124, 1810

Sun A.-L., Greene J. E., Zakamska N. L., 2017, ApJ, 835, 222

Sutherland R., Dopita M., Binette L., Groves B., 2018, Astrophysics Source Code Library, record ascl:1807.005

Theureau G., Hanski M. O., Coudreau N., Hallet N., Martin J. M., 2007, A&A, 465, 71

Torres-Flores S., Amram P., Mendes de Oliveira C., Plana H., Balkowski C., Marcelin M., Olave-Rojas D., 2014, MNRAS, 442, 2188

Torrey P., Cox T. J., Kewley L., Hernquist L., 2012, ApJ, 746, 108

Treister E., Schawinski K., Urry C. M., Simmons B. D., 2012, ApJ, 758, L39

Trippe M. L., Crenshaw D. M., Deo R., Dietrich M., 2008, AJ, 135, 2048

Ulvestad J. S., Wilson A. S., 1984, ApJ, 285, 439

Veilleux S. et al., 2013, ApJ, 776, 27

Veilleux S., Osterbrock D. E., 1987, ApJS, 63, 295

Veilleux S., Shopbell P. L., Miller S. T., 2001, AJ, 121, 198

Veron P., Lindblad P. O., Zuiderwijk E. J., Veron M. P., Adam G., 1980, A&A, 87, 245
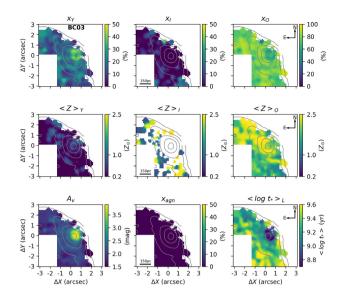
Villar-Martín M., Humphrey A., Delgado R. G., Colina L., Arribas S., 2011, MNRAS, 418, 2032

Ward M., Penston M. V., Blades J. C., Turtle A. J., 1980, MNRAS, 193, 563

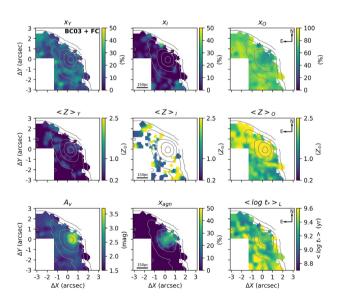Wilkinson D. M., Maraston C., Goddard D., Thomas D., Parikh T., 2017, MNRAS, 472, 4297

Zakamska N. L. et al., 2016, MNRAS, 459, 3144

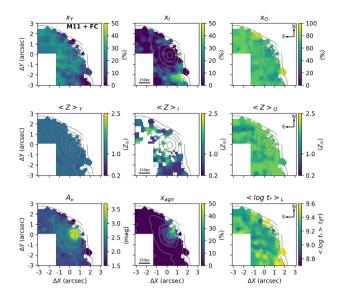## APPENDIX A: STELLAR POPULATIONS SYNTHESIS MAPS

We show the maps of the recovered properties from three spatially resolved STARLIGHT synthesis we have performed, namely *BC03*, *BC03 + FC*, and *M11 + FC*. The top panels show, from left to right, the per cent contribution to the total light for young, intermediate, and old SSPs (x_Y, x_I, and x_O). In the middle panels, the light-weighted mean stellar metallicity for the three age groups, from left to right, $\langle Z \rangle_Y$, $\langle Z \rangle_I$, and $\langle Z \rangle_O$. In the bottom panel, the *V*-band extinction (A_V), the per cent contribution to the total light from the FC component (x_{agn}), and the light-weighted mean stellar age, $\langle \log t_* \rangle$, are shown, respectively, from left to right.

Figure A1. Maps of the recovered properties from the *BC03* synthesis. Top: from left to right, percentage contribution to the total light from young, intermediate, and old SSPs (x_Y, x_I, and x_O). Middle: from left to right, light-weighted mean stellar metallicity for the three SSP age groups, $\langle Z \rangle_Y$, $\langle Z \rangle_I$, and $\langle Z \rangle_O$. Bottom left: A_V extinction parameter. Bottom middle: Featureless continuum (FC) component percentage contribution to the total light (x_{agn}). Bottom right: Light-weighted mean stellar age, $\langle \log t_* \rangle$. The grey contour in all the maps is the continuum emission (left-hand panel of Fig. 1). The x_{agn} is null in all points by definition, because there is no FC component in *BC03* synthesis spectra base.
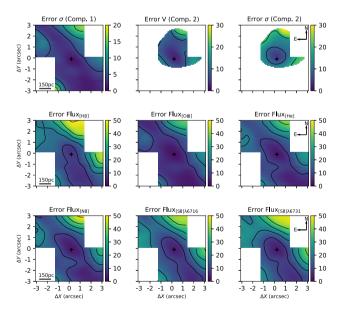

Figure A2. Same as Fig. A1 for *BC03 + FC*.

Figure A3. Same as Fig. A1 for *M11 + FC*.

APPENDIX B: EMISSION-LINE FITTING UNCERTAINTIES

We present here the uncertainties in the parameters of the emission lines fitting described in Section 4.1. The uncertainties are the standard deviation over the 100 Monte Carlo iterations. The uncertainties in the radial velocity (V) of Component 1 were already presented in Fig. 8. In Fig. B1, we show the uncertainties in the velocity dispersion (σ) of Component 1, the values are mostly smaller than 5 km s^{-1}, reaching a maximum value of 15 km s^{-1}.

Figure B1. Emission-line fitting uncertainties. Top: from right to left, velocity dispersion of Component 1 (km s^{-1}), radial velocity of Component 2 (km s^{-1}), and velocity dispersion of Component 2 (km s^{-1}). Middle and bottom: percentage uncertainties in the integrated flux (Component 1 + Component) of Hβ, [O III]λ5007, Hα, [N II]λ6583, and [S II]λ6716,6731 (per cent). The black cross shows the peak of the continuum emission. Each contour in the maps means a 10 per cent variation in the uncertainties.

In the top panel, we also show the uncertainties of v and σ of Component 2, values are less than 10 km s^{-1} in most the region, reaching up to 30 km s^{-1} in a very small region, the σ values are less than 10 km s^{-1} in the peak of component emission and up to 30 km s^{-1} in the borders of the detection region. In the middle and bottom panels, the percentile uncertainties in the integrated flux (Component 1 + Component 2) of Hβ, [O III]λ5007, Hα, [N II]λ6583, and [S II]λ6716,6731 are shown.
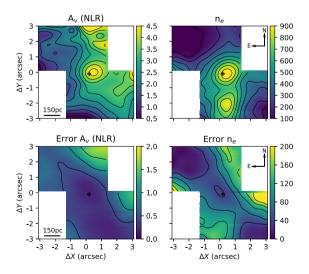
The Hβ line uncertainties range from 10 per cent at the centre of the FoV, up to 45 per cent in the dust lane region. [O III] and Hα values range from less than 5 per cent up to 25 per cent at the dust lane region. [S II] and [N II] values range from less than 10 per cent up to 35 per cent at the dust lane region.

APPENDIX C: NEBULAR EXTINCTION AND ELECTRON DENSITY

In order to measure the extinction in the NLR, we adopt the Calzetti et al. (2000) extinction law, and assume the case B recombination and the intrinsic Hα/Hβ value for the NLR (Osterbrock & Ferland 2006), which combined leads to the following expression to the *V*-band extinction:

$$A_V = 7.95 \times \log_{10} \left(\frac{\mathrm{H}\alpha/\mathrm{H}\beta}{3.1} \right). \tag{C1}$$

In order to improve the S/N and given the fact that Hβ Component 2 is detected in a very small region, we used the integrated flux (Component 1 + Component 2) of the NLR Hα and Hβ lines. The A_V map is presented in the top left panel of Fig. C1, and its uncertainty in the bottom left panel. The A_V peak at ~4.5 mag at the peak of the emission lines emission, and has values > 3.5 mag in the dust lane portion of the FoV. However, this value may be even higher as the uncertainties are up to 2 mag in this region, caused by high impression on the Hβ flux measurement, as seen in Fig. B1. Although the A_V are not the same in the continuum Appendix A and in the NLR, the spatial patterns are similar: the higher values are found the central spaxels and towards the dust lane, and the lower towards the SE direction.

Figure C1. Top left and bottom left panels shows, respectively, the *V*-band extinction A_V map and its uncertainties, both in units of magnitudes. Top right and bottom right panel show, respectively, the electron density (n_e) and its uncertainties both in cm^{-3} units. The black cross shows the peak of the continuum emission.

The electron density (n_e) of the ionized gas in the NLR can be obtained from the ratio between the [S II] lines, [S II]$\lambda 6716/\lambda 6731$ (Osterbrock & Ferland 2006). We applied the solution of the collisional equilibrium equations given by Proxauf, Öttl & Kimeswenger (2014) to obtain the n_e values as follows:

$$\log_{10}(n_e \, [\mathrm{cm}^3]) = 0.0543 \tan(-3.0553R + 2.8506) + 6.98$$
$$- 10.6905R + 9.9186R^2 - 3.5442R^3 \qquad (C2)$$

with $R = F_{6716}/F_{6731}$, the ratio between the [S II] lines. The n_e map in its uncertainties are presented, respectively, in the top right and bottom right panel of Fig. C1. The maximum value of n_e is 950 cm^{-3} reached at the peak of the emission lines, decreasing radially down to 100 cm^{-3}, another high-density ($\sim$800 cm^{-3}) knot is present at the south of the nucleus. Both the values as well as the spatial profiles of both A_V and n_e measured here are in agreement with the recent published analyses by Mingozzi et al. (2019) using MUSE instrument (see their figs A1 and B1).

This paper has been typeset from a TEX/LATEX file prepared by the author.